Monthly Notices of the ROYAL ASTRONOMICAL SOCIETY

MNRAS **503,** 4320–4335 (2021) doi:10.1093/mnras/stab700
Advance Access publication 2021 March 22

ALMA–IRDC – II. First high-angular resolution measurements of the $^{14}N/^{15}N$ ratio in a large sample of infrared-dark cloud cores

F. Fontani [1,2★] A. T. Barnes [3] P. Caselli,[2] J. D. Henshaw [4] G. Cosentino [5] I. Jiménez-Serra,[6] J. C. Tan,[5] J. E. Pineda [2] and C. Y. Law[5]

[1]*INAF-Osservatorio Astrofisico di Arcetri, Largo E. Fermi 5, I-50125 Florence, Italy*
[2]*Centre for Astrochemical Studies, Max-Planck-Institute for Extraterrestrial Physics, Giessenbachstrasse 1, D-85748 Garching, Germany*
[3]*Argelander Institute for Astronomy, University of Bonn, Auf dem Hügel71, D-53121 Bonn, Germany*
[4]*Max Planck Institute for Astronomy, Königstuhl 17, D-69117 Heidelberg, Germany*
[5]*Space, Earth and Environment Department, Chalmers University of Technology, Chalmersplatsen 4, SE-41296 Göteborg, Sweden*
[6]*Departamento de Astrofísica, Centro de Astrobiología, E-28850 Torrejón de Ardoz, Madrid, Spain*

Accepted 2021 March 5. Received 2021 March 5; in original form 2020 October 9

ABSTRACT

The $^{14}N/^{15}N$ ratio in molecules exhibits a large variation in star-forming regions, especially when measured from N_2H^+ isotopologues. However, there are only a few studies performed at high-angular resolution. We present the first interferometric survey of the $^{14}N/^{15}N$ ratio in N_2H^+ obtained with Atacama Large Millimeter Array observations towards four infrared-dark clouds harbouring 3 mm continuum cores associated with different physical properties. We detect $N^{15}NH^+$ (1–0) in $\sim$ 20–40 per cent of the cores, depending on the host cloud. The $^{14}N/^{15}N$ values measured towards the millimetre continuum cores range from a minimum of $\sim$80 up to a maximum of $\sim$400. The spread of values is narrower than that found in any previous single-dish survey of high-mass star-forming regions and than that obtained using the total power data only. This suggests that the $^{14}N/^{15}N$ ratio is on average higher in the diffuse gaseous envelope of the cores and stresses the need for high-angular resolution maps to measure correctly the $^{14}N/^{15}N$ ratio in dense cores embedded in IRDCs. The average $^{14}N/^{15}N$ ratio of $\sim$210 is also lower than the interstellar value at the Galactocentric distance of the clouds ($\sim$300–330), although the sensitivity of our observations does not allow us to unveil $^{14}N/^{15}N$ ratios higher than $\sim$400. No clear trend is found between the $^{14}N/^{15}N$ ratio and the core physical properties. We find only a tentative positive trend between $^{14}N/^{15}N$ and H_2 column density. However, firmer conclusions can be drawn only with higher sensitivity measurements.

Key words: stars: formation – ISM: clouds – ISM: molecules.

1 INTRODUCTION

Nitrogen, the fifth most abundant element in the Universe, has two stable isotopes: ^{14}N and ^{15}N. In the Solar System, the nitrogen isotopic fraction, $^{14}N/^{15}N$, shows variations of an order of magnitude, from $\sim$50 in carbonaceous chondrites (Bonal et al. 2010) to $\sim$130–160 in comets (Bockelée-Morvan et al. 2008; Manfroid et al. 2009; Shinnaka et al. 2016), up to $\sim$450 in the atmosphere of Jupiter (Fouchet et al. 2004) and in the Solar wind ($\sim$441, Marty et al. 2010). The latter, in particular, is believed to represent the proto-Solar nebula (PSN) value (Füri & Marty 2015). This indicates an enrichment in ^{15}N in pristine Solar System small bodies, but the causes of this enrichment, and in particular its relation with the chemical evolution of the PSN, are not yet understood.

In the past, a popular explanation for the ^{15}N enrichment has been the isotopic exchange reactions occurring at low temperatures (Terzieva & Herbst 2000; Rodgers & Charnley 2008), similar to those at the origin of molecular deuterium enrichment in cold dense cores (e.g. Ceccarelli et al. 2014 and references in there). This explanation has been challenged by theoretical works which have excluded low-temperature reactions as the main way to enhance ^{15}N in molecular species (e.g. Wirström et al. 2012; Roueff, Loison & Hickson 2015; Wirström & Charnley 2018, Loison et al. 2019), and have also excluded significant nitrogen fractionation (both ^{15}N enrichment and depletion) in the most abundant molecules during the chemical evolution of a star-forming core. Significant variations in nitrogen fractionation are theoretically predicted only in extragalactic environments strongly affected by high fluxes of cosmic rays (Viti et al. 2019). However, these predictions are at odds with the large variations of $^{14}N/^{15}N$ measured in star-forming cores. In fact, in low-mass pre-stellar cores the $^{14}N/^{15}N$ ratio measured from N_2H^+ varies from $\sim$330 (Daniel et al. 2013, 2016) to $\sim$1000 (Bizzocchi et al. 2013; De Simone et al. 2018; Furuya et al. 2018; Redaelli et al. 2018), namely up to more than twice the PSN value, indicating a depletion rather than an enrichment of ^{15}N. This depletion has been proposed to be due to the transition from atomic to molecular nitrogen in the earlier evolutionary stage of the cores by Furuya & Aikawa (2018), although their models are not able to reach the antifractionation levels measured in pre-stellar cores. Some works (Loison et al. 2019; Hily-Blant et al. 2020) propose that only a different dissociative recombination rate for N_2H^+ and $N^{15}NH^+$

★ E-mail: francesco.fontani@inaf.it

could solve the problem and reconcile observations with chemical models, although it is hard to understand what could cause the different rate for the two species. On the other hand, in CN and HCN the $^{14}N/^{15}N$ ratio seems more consistent with the PSN value (Hily-Blant et al. 2013a,b). In protoplanetary disks, the $^{14}N/^{15}N$ is found to be ∼83–156 (Guzmán et al. 2017) from observations of HCN isotopologues, while in TW Hya from CN is ∼323 (Hily-Blant et al. 2017), i.e. in between the PSN and the cometary values. Overall, these findings suggest a high variability of the $^{14}N/^{15}N$ ratio, which depends on both the evolutionary stage of the source and the molecule observed.

Besides low-mass star-forming cores, a growing observational effort has been devoted to the study of the $^{14}N/^{15}N$ ratio in high-mass star-forming regions, based on the evidence that the Sun was likely born in a crowded stellar cluster including stars more massive than ∼8 $M_\odot$ (e.g. Adams 2010; Pfalzner et al. 2015; Lichtenberg et al. 2019). Traces of the interaction between these stars and the primordial Solar System are recorded in meteoritic material, where anomalous high abundances of daughter species of Short-Lived Radionucleides (SLRs), produced by nearby high-mass stars and ejected during the early evolution of the Solar System, are measured (e.g. Portegies Zwart et al. 2018). Therefore, the birthplaces of massive stars and clusters are ideal targets to investigate the relation between the ^{15}N enrichment in pristine Solar System material and its birth environment.

Even in this case, single-dish surveys of massive star-forming regions indicate large variations in the $^{14}N/^{15}N$ ratio. The highest variability is found, again, in N_2H^+ (∼180–1300, Fontani et al. 2015), while values distributed in between the cometary values and the PSN one are found in CN, HCN, and HNC (Adande & Ziurys 2012; Fontani et al. 2015; Zeng et al. 2017; Colzi et al. 2018a, b). The previous studies also suggest that the evolution does not seem to play a role, in agreement with the predictions of models (e.g. Roueff et al. 2015), although they cannot predict the broad measured range of isotopic ratios. However, the observations mentioned above were obtained with single-dish telescopes, thus providing average values of the $^{14}N/^{15}N$ ratio on linear scales of ∼0.1–1 pc, which can contain gas with different conditions, due to the inner physical and chemical complexity of high-mass star-forming cores. Hence, these observations could miss the presence of spots enriched (or depleted) in ^{15}N on linear scales ≤0.1 pc, i.e. smaller than the telescope beam.

The few follow-up observations performed at high-angular resolution have indeed suggested that local gradients in the $^{14}N/^{15}N$ ratio can be found at smaller linear scales: Colzi et al. (2019) have observed the high-mass protocluster IRAS 05358 + 3543 with a linear resolution of ∼0.05 pc, or ∼10000 au, and found that the $^{14}N/^{15}N$ ratio in N_2H^+ shows an enhancement of a factor ∼2 (from ∼100–220 to ≥200) going from the inner dense core region to the diffuse, pc-scale, envelope, and interpreted these results as the consequence of selective photodissociation (Heays et al. 2014; Lee et al. 2021). The latter mechanism, due to self-shielding of $^{14}N_2$, for N_2H^+ predicts a decrease of the $^{14}N/^{15}N$ ratio in regions exposed to external UV irradiation, as indeed found by Colzi et al. (2019). On the other hand, in embedded, not irradiated regions, the $^{14}N/^{15}N$ ratio in N_2H^+ should not change, and this has been recently confirmed by observations with linear resolution of ∼600 au of the protocluster OMC–2 FIR4, which have revealed a constant $^{14}N/^{15}N$ in the embedded protocluster cores (Fontani et al. 2020). However, these are, at present, the only two studies performed at high-angular resolution in high-mass star-forming regions, and the results need to be corroborated by similar studies both towards other sources and in different molecules.

When investigating the birthplace of massive stars, infrared-dark clouds (IRDCs) are certainly ideal targets. IRDCs are cold ($T \leq 25$ K; Pillai et al. 2006), dense ($n(H_2) \geq 10^{4-5}$ cm^{-3}) and highly-extinguished ($A_v \geq 100$ mag and $N(H_2) \geq 10^{22}$ cm^{-2}; Butler & Tan 2009, 2012) molecular clouds, first observed in extinction against the bright mid-IR Galactic background (Perault et al. 1996; Egan et al. 1998). Despite their importance for star-formation, they have been poorly investigated so far in nitrogen fractionation. Zeng et al. (2017) measured with the IRAM-30m telescope the $^{14}N/^{15}N$ towards cores belonging to four IRDCs from HCN and HNC, and found once more a large variability ($^{14}N/^{15}N$ ∼70–800 in HCN and ∼161–541 in HNC), with the lowest values belonging to the lowest density regions. But, again, these are average values over ∼0.5–1 pc linear scales that encompass gas with different physical and chemical properties. Moreover, these measurements also depend on the $^{13}C/^{12}C$ ratio, which has been found to be affected by physical conditions as well as time evolution (Colzi et al. 2020).

In this paper, we present the first interferometric study of the $^{14}N/^{15}N$ ratio towards a large sample of IRDC cores in N_2H^+ at high-angular resolution. The $^{14}N/^{15}N$ ratio is derived from observations of N_2H^+ and $N^{15}NH^+$ (1–0) towards the dense cores of four clouds in which the physical and chemical structure has already been extensively studied at various wavelengths, from the mid-infrared to the submillimetre (Butler & Tan 2009, 2012; Hernandez et al. 2011; Henshaw et al. 2014; Jiménez-Serra et al. 2014; Barnes et al. 2016), both with single-dish telescopes and interferometers, allowing us to put in relation the $^{14}N/^{15}N$ ratios with the core properties. In particular, because each core is classified as starless or star-forming within each cloud, we are also able to compare the $^{14}N/^{15}N$ ratios with the presence/absence of protostellar activity. Observations and data reduction are described in Section 2. The results are shown in Section 3, and discussed in Section 4. The main findings of this work and the implications for follow-up studies are presented in Section 5.

2 OBSERVATIONS AND DATA REDUCTION

Observations have been performed with the Atacama Large Millimeter Array (ALMA) towards the sample of IRDCs described in Barnes et al. 2021 (hereafter paper I). The project IDs are 2017.1.00687.S and 2018.1.00850.S (PI: A.T. Barnes). We refer to that work for the complete source sample description and for any observational detail. In this paper we analyse only the four IRDCs detected in $N^{15}NH^+$ (1–0) listed in Table 1, in which we also give some source properties, as well as important observational parameters (angular resolution, spectral resolution, 1σ rms noise in the final clean cubes). Spectroscopic parameters of the two lines analysed, i.e. N_2H^+ and $N^{15}NH^+$(1–0), are reported in Table 2, together with relevant observational parameters (i.e. sensitivity and spectral/angular resolution). Calibration, imaging, and deconvolution of the interferometric data were performed with the Common Astronomy Software Calibration (CASA) package[1] (McMullin et al. 2007), using the CASA-PIPELINE (version: 5.4.0-70). Continuum subtraction was performed by taking the line-free channels around the lines in

[1]CASA is developed by an international consortium of scientists based at the National Radio Astronomical Observatory (NRAO), the European Southern Observatory (ESO), the National Astronomical Observatory of Japan (NAOJ), the Academia Sinica Institute of Astronomy and Astrophysics (ASIAA), the CSIRO division for Astronomy and Space Science (CASS), and the Netherlands Institute for Radio Astronomy (ASTRON) under the guidance of NRAO. See https://casa.nrao.edu

Table 1. Clouds with clear detections in $N^{15}NH^+$(1–0) and main observational parameters: coordinates of map centre, systemic velocity (V_{sys}), heliocentric distance (d), channel width in velocity (ΔV), synthesized beam (θ_{SB}), and root-mean-square noise per channel (1σ).

Cloud	ID	R.A. (J2000) h: m: ″	Dec. (J2000) °: ′: ″	V_{sys} (km s^{-1})	d (kpc)	ΔV^a (km s^{-1})		θ_{SB} (″)		1σ (mJy beam^{-1})	
						N_2H^+	$N^{15}NH^+$	N_2H^+	$N^{15}NH^+$	N_2H^+	$N^{15}NH^+$
C	G028.37 + 00.07	18:42:50.03	–04:03:23.4	78	5.0	∼0.05	∼0.1	3.5″ × 3.1″	3.5″ × 3.2″	∼11	∼9
D	G028.53–00.25	18:44:16.94	–03:59:40.8	86	5.7	∼0.05	∼0.1	3.8″ × 3.0″	3.8″ × 3.1″	∼12	∼9
F	G034.43 + 00.24	18:53:18.43	+ 01:27:13.5	57	3.7	∼0.05	∼0.1	3.9″ × 3.1″	4.0″ × 3.1″	∼11	∼9
H	G035.39–00.33	18:57:09.42	+ 02:08:05.4	43	2.9	∼0.05	∼0.1	3.4″ × 3.0″	3.4″ × 3.1″	∼12	∼9

[a]The spectral resolution of the clean cubes corresponds to twice the channel spacing (ΔV).

Table 2. Spectroscopic parameters of the observed lines: rest frequency (ν_0), energy of the upper level (E_u), degeneracy of the upper level (g_u), Einstein coefficient for spontaneous emission (A_{ul}).

Transition	Hyperfine component	ν_0 (MHz)	E_u[(a)] (K)	g_u[(a)]	A_{ul}[(a)] (s^{-1})
N_2H^+ (1–0)	$F_1 = 1 - 1$	93171.88[(a)]	4.47	9	3.63×10^{-5}
	$F_1 = 2 - 1$	93173.70[(a)]		15	
	$F_1 = 0 - 1$	93176.13[(a)]		3	
$N^{15}NH^+$ 1–0	F =1 − 1	91204.26[(b)]	4.33	3	3.40×10^{-5}
	F = 2 − 1	91205.99[(b)]		5	
	F = 0 − 1	91208.52[(b)]		1	

[a]From the Cologne Database for Molecular Spectroscopy (CDMS; Endres et al. 2016);
[b]From Dore et al. (2009).

each individual spectral window (the results of the pipeline were checked), and subtracted from the data directly in the *(u,v)*-domain. The maximum recoverable scale was set by the size of the smallest 7 m baseline of 8.9 m, which corresponds to ∼70 arcsec at 93.2 GHz. Therefore, complementary total power observations were taken to recover the zero-spacing for the molecular lines. These single-dish observations were also reduced using the CASA-PIPELINE tool (version: 5.4.0-70). The 12 m, 7 m, and total power observations were combined using the FEATHER function in CASA (version 4.7.0) with the default parameter set (i.e. effective dish size, single-dish scaling, and low-pass filtering of the single-dish observations). Clean cubes extracted around the lines of interest were then converted into fits format and further analysed with packages of the GILDAS[2] software. In particular, the spectra of N_2H^+ and $N^{15}NH^+$(1–0) were extracted with MAPPING, and analysed in the way described in Section 3 with CLASS.

3 RESULTS

The $N^{15}NH^+$(1–0) has been detected towards several positions in the four clouds in Table 1 with signal-to-noise ratio in the range ∼3–7. The N_2H^+(1–0) line was clearly detected with excellent signal to noise (≥20) in all clouds (see Figs A-1–A-4) after smoothing to a uniform spectral resolution of ∼0.4 km s^{-1}. Due to the faintness of the $N^{15}NH^+$ lines, we do not show integrated maps of the $N^{15}NH^+$ emission.

The faintness of the $N^{15}NH^+$ emission, and the large angular extension and morphological complexity of the target clouds, suggested us to focus the $^{14}N/^{15}N$ analysis first on the 3 mm continuum sources identified in each IRDC using the 2D dendrogram method (Rosolowsky et al. 2008). The parameter set and method for determination of the continuum dendrogram structure is described in paper I. The continuum sources are shown in Fig. 1. We point out that the choice of the input parameters in the dendrogram analysis does not significantly affect the identification of the cores as demonstrated in paper I. These sources are well characterized from the dynamical and evolutionary point of view, and hence will allow us to discuss the $^{14}N/^{15}N$ ratio based on the core properties in Section 4. In particular, the cores have been classified as starless or star forming based on the identification of an infrared source inside the core boundaries (paper I).

We also extracted and analysed spectra from the N_2H^+ intensity peaks to derive the $^{14}N/^{15}N$ ratio towards these peaks. These have been identified here by conducting the dendrogram analysis on the (2D) integrated intensity maps of N_2H^+ (see paper I). The following set of parameters is used for determination of the dendrogram structure: MIN_VALUE $= 30\sigma \sim 4.5$ K kms (the minimum intensity considered in the analysis); MIN_DELTA $= 30\sigma$ (the minimum spacing between isocontours); MIN_PIX $= 3$ beam $\sim$ 150 pixels (the minimum number of pixels contained within a structure). Given the complex and extended morphology of the N_2H^+ emission, more stringent dendrogram criteria were imposed compared to the continuum. This parameter set produced a simplistic dendrogram hierarchy, which was preferred as this work focuses on the detection and analysis of the weak ^{15}N emission, as opposed to a rigorous classification of the structures seen in N_2H^+ emission.

For simplicity, in the following we will call 'cores' the N_2H^+ intensity peaks identified in this way as well. These N_2H^+ cores are typically larger (i.e. more diffuse) than the continuum cores, due to the difference in dendrogram parameters. The N_2H^+ emission morphology is shown in Fig. 2, in which we plot for each cloud the peak intensity of the N_2H^+(1–0) line superimposed on the mass (H_2) surface density map, Σ, obtained from combined Spitzer near- and mid-infrared extinction maps (Kainulainen & Tan 2013): overall, the Σ morphology matches well the N_2H^+ emission peak in Cloud C, F, and H, even though the peaks of the two tracers coincide relatively well only in Cloud C, while in cloud H and F some N_2H^+ peaks are not coincident with the Σ peaks. This apparent disagreement between the N_2H^+(1–0) intensity peak and Σ peaks, especially in Cloud D and partly also in Cloud H and F, could be due to several causes affecting the N_2H^+ line profile in the regions with high extinction. Indeed, as we will discuss in Section 3.1.3, the N_2H^+ spectra show a very complex profile suggestive of multiple velocity components, self-absorption, and high-optical depth effects, in particular towards Cloud D and H.

The contours used for the extraction of the spectra are shown in Fig. 1, where we can note that several continuum cores are superimposed, or totally included, in the N_2H^+ cores. However, the

[2]https://www.iram.fr/IRAMFR/GILDAS/

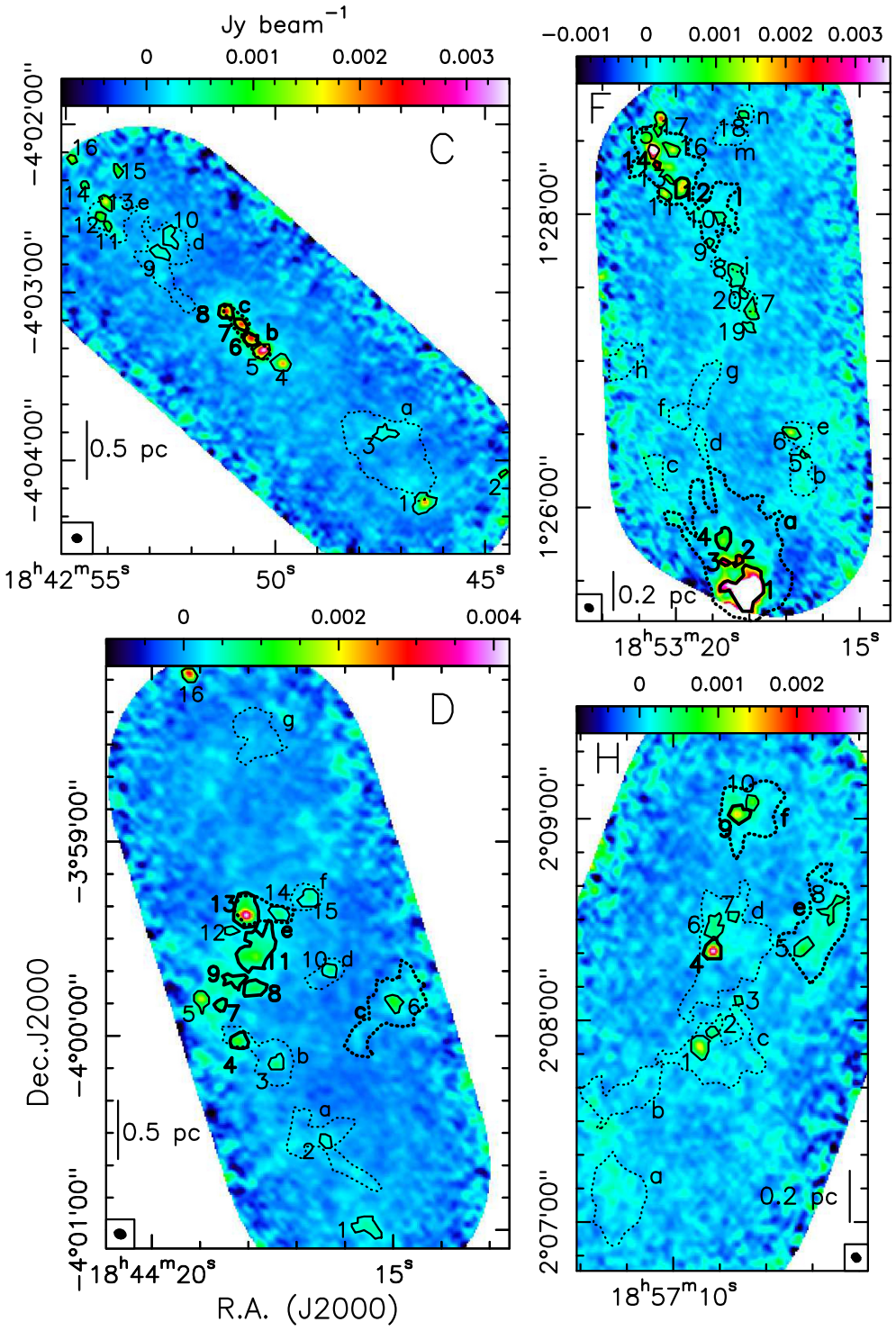

Figure 1. Continuum maps of the four target clouds, in Jy beam^{-1} units. The solid and dotted contours illustrate the continuum and N_2H^+ cores, respectively, derived in paper I from the dendrogram analysis. In both cases, the thick contours indicate the cores detected in $N^{15}NH^+$ (1–0). The numbers and letters correspond to the core IDs defined in the last column of Tables 3 and 4. In each frame, the ellipse in the bottom left (right for Cloud H) corner is the ALMA synthesized beam, and the vertical solid line shows a linear scale of 0.5 pc for cloud C and D, and 0.2 pc for cloud F and H.

N_2H^+ cores are usually more extended, and in some cases they are not detected in the 3 mm continuum, and vice-versa. A similar feature was found by Di Francesco et al. (2004) in Oph A, and interpreted as being due to the fact that N_2H^+ (1–0) is tracing the cold gas better than the dust continuum emission, which is biased toward warm regions. Therefore, our 'double' analysis allows us to investigate if the $^{14}N/^{15}N$ ratios change from the compact continuum cores to the more diffuse N_2H^+ ones.

We will present first the results of the data analysis of the spectra extracted from the continuum cores in Section 3.1, and then we will show those obtained from the N_2H^+ cores in Section 3.2, also comparing the two results.

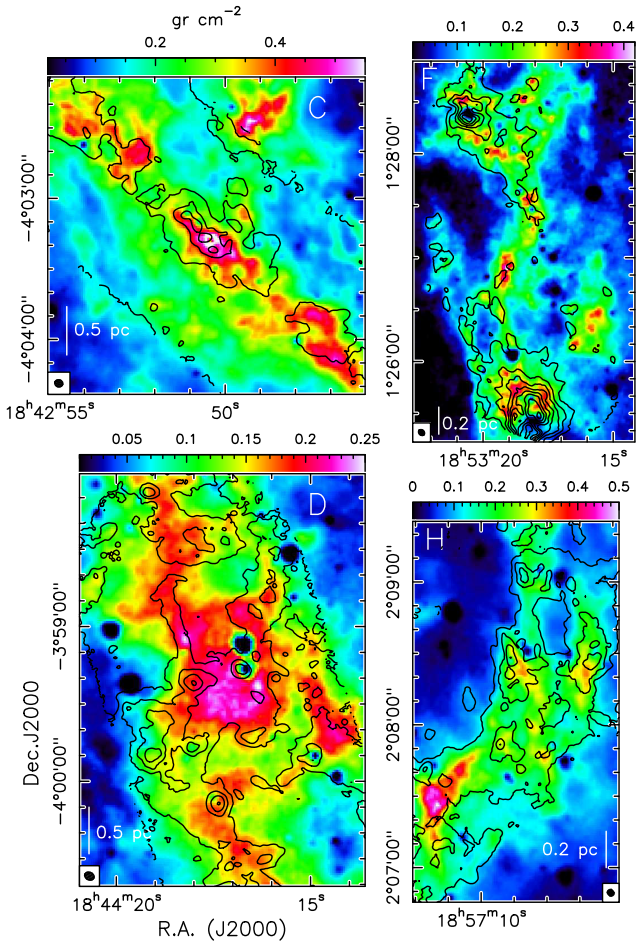

Figure 2. Mass (H_2) surface density maps, Σ, of the four target clouds (in g cm^{-2} units, colour scale, Kainulainen & Tan 2013) superimposed on the N_2H^+(1–0) line emission peak (solid contours), in brightness temperature units, obtained with ALMA (paper I). In each frame, first contour and step are the 3σ rms level of the N_2H^+(1–0) peak map (2.7 K for Cloud C; 1.4 for Cloud D; 2.7 K for Cloud F; 1.5 K for Cloud H), the ellipse in the bottom left (right for Cloud H) corner is the ALMA synthesized beam, and the vertical solid line shows a reference linear scale.

3.1 Spectra towards the 3 mm continuum cores

3.1.1 Extraction of the spectra and line detection

We extracted $N^{15}NH^+$(1–0) spectra from the continuum sources identified in paper I, and detected significant emission towards three cores in Cloud C ($\sim$ 19 per cent), six cores in Cloud D ($\sim$ 38 per cent), six cores in Cloud F ($\sim$ 30 per cent), and two cores in Cloud H ($\sim$ 20 per cent). The contours used for the extraction of the spectra are shown in Fig. 1, where we highlight the cores detected in $N^{15}NH^+$. The integrated flux density, F_ν, of each spectrum has been converted to brightness temperature units via the formula:

$$T_B(K) \simeq 1222 F_\nu(\mathrm{mJy})/[\nu^2(\mathrm{GHz})\Theta^2(\mathrm{arcsec})] \,, \quad (1)$$

where ν is the rest frequency of the transition (see Table 2) and Θ is the observed angular equivalent diameter (i.e. the diameter of the equivalent circle) of each core (paper I). Therefore, T_B is an average brightness temperature over the angular surface of each core. We stress that equation (1) is valid also for non-spherical sources as long as Θ is the source equivalent angular diameter. Following the same approach, we will have extracted and analysed spectra from the N_2H^+ cores, which will be discussed in Section 3.2

The spectra in T_B units are shown in Figs A-1–A-4. The $N^{15}NH^+$ emission is preferentially detected towards cores with strong continuum emission (cores C2c3/5, C2c4, and C2c6 in Cloud C; core D7c3 in Cloud D; Cores F1c1, F1c2, F1c3, F4c5, and F4c7 in Cloud F; cores H3c3 and H5c3 in Cloud H), and are usually located in the central part of the cloud, with the exception of the cores in Cloud F, located at the southern and northern edge of the cloud (Fig. 1).

3.1.2 Line fits: $N^{15}NH^+$ (1–0)

The $N^{15}NH^+$ (1–0) line possesses hyperfine structure due to the nuclear spin of the ^{14}N nucleus, which splits the transition in three components well separated in frequency, with the strongest one at the centre of the spectrum, and two fainter satellites. The frequencies of the components and relevant spectroscopic parameters are given in Table 2. In all but four cores, D5c5/6/7, F1C3, F4c5, and F4c7, the hyperfine structure cannot be fitted because the satellites are undetected. Therefore, the main components have been fitted with a single Gaussian, except in the four cores mentioned above, for which we have fitted simultaneously all components using the CLASS software (method hfs in CLASS): the method considers that the velocity separation of the components is fixed to the laboratory values, and that all components have the same excitation temperature (T_{ex}) and the same line full width at half-maximum (FWHM).

By fitting a single Gaussian to the lines in which only the main hyperfine component is detected, we are underestimating the total line integrated area. To compute the total column density we have appropriately derived the total integrated intensity from our partial estimates as explained in Section 3.1.4.

3.1.3 Line fits: N_2H^+(1–0)

The N_2H^+ (1–0) has also hyperfine structure with 15 components, of which seven are resolved in velocity in quiescent cores (see e.g. Caselli, Myers & Thaddeus 1995). However, in many observed spectra, including ours, the line widths are much larger than the separation in velocity of the components, which are thus grouped in three spectral features (Figs A-1–A-4). Moreover, the profile is often complex and difficult to fit even considering the hyperfine structure. Such complexity can be attributed to multiple velocity components, known to be present in the targets (e.g. Henshaw et al. 2013, 2014; Barnes et al. 2018), and/or to optical depth effects and self-absorption.

Let us discuss now in detail the profiles of the N_2H^+ (1–0) lines in each cloud. We examine in particular the spectra of the cores also detected in $N^{15}NH^+$ (1–0), from which we will compute the $^{14}N/^{15}N$ ratios:

(i) Cloud C: all spectra show a main component centred at (or very close to) the systemic velocity of the cloud ($\sim$78 km s^{-1}), and a fainter redshifted emission, most apparent in, e.g. C1c1, C2c1, and C2c2 (Fig. A-1). The redshifted emission is also clearly apparent in the three cores detected in $N^{15}NH^+$, i.e. C2c3/5, C2c4, and C2c6. In particular, in C2c3/5 and C2c4 the central velocity of the main component is displaced by $\sim$1 km s^{-1} with respect to the $N^{15}NH^+$ (1–0) line peak, suggesting that self-absorption could cause the asymmetric profile of N_2H^+(1–0). Moreover, the FWHM of the $N^{15}NH^+$ (1–0) lines are narrower than those of N_2H^+(1–0), which again could be due either to self-absorption in the main isotopologue line, or to multiple overlapping velocity features,

undetected in $N^{15}NH^+$ (1–0) because too faint. To understand which of these two phenomena produces more likely the observed line features in N_2H^+ and $N^{15}NH^+$, we have first performed a fit with two velocity components in N_2H^+, which gives good results in the three cores. Then, we have compared the $N^{15}NH^+$ line velocity peak with that of the two candidate velocity features in the isolated hyperfine component $F_1 = 0 - 1$ of N_2H^+(1–0): we found that the peak of the strongest velocity feature in N_2H^+ coincides within the uncertainties with the $N^{15}NH^+$ velocity peak, favouring, for N_2H^+(1–0), the multiple velocity component hypothesis with respect to self-absorption;

(ii) Cloud D: this is the cloud with the most complex spectral features. Fits to the line profiles even including multiple velocity components and high optical depths provide high residuals in the six cores detected in $N^{15}NH^+$, i.e. D6c4, D6c6, D7c1, D7c2, D5c5/6, and D8c1. As for Cloud C, the displacement of $\sim$1 km s^{-1} or more between the peaks of the $N^{15}NH^+$ (1–0) and the velocity peak of the main component of N_2H^+(1–0) suggests that self-absorption can be important. But multiple velocity components, undetected in $N^{15}NH^+$ (1–0), cloud also contribute to the total line profile. As for Cloud C, we have compared the peak velocity of $N^{15}NH^+$(1–0) with the possible velocity features in the $F_1 = 0 - 1$ component of N_2H^+(1–0), and found that in three cases, i.e. D6c6, D7c1, and D7c2, the peak velocity of the $N^{15}NH^+$(1–0) sits in between the peaks of the two velocity feature candidates seen in N_2H^+ (see Fig. A-2). Therefore, in these cores the N_2H^+ asymmetric line profile is likely due to self-absorption. In the other three cores, i.e. D6c4, D5c5/6, and D8c1, the profile may be due to two velocity features;

(iii) Cloud F: The lines can be fitted with a single velocity component in all spectra except that in F1c5, F1c6, F2c1, and F2c2, where there seem to be at least two velocity components (Fig. A-3). Among the five cores detected in $N^{15}NH^+$ (1–0), i.e. F1c1, F1c2, F1c3, F1c4, F4c5, and F4c7, only F1c2 and F1c3 show hints of a secondary blueshifted velocity feature. However, in both cases the $N^{15}NH^+$ line peaks sit neither in between the possible two velocity features nor on one of them precisely, and hence one cannot establish which is the (main) cause of the asymmetric profile in N_2H^+. Nevertheless, these possible secondary velocity features contribute to the integrated intensity by less than 20 per cent (A-3), and hence does not affect strongly the integrated intensity estimate;

(iv) Cloud H: the line profiles are very different among the various cores (A-4), going from single velocity components with moderate (H3c3) or high (H5c3, H5c1) optical depth, to multiple velocity features (H2c1, H4c1, H3c1). Again, the profile of the isolated $F_1 = 0 - 1$ hyperfine component is the least affected and is well fitted by a single Gaussian in the two cores detected in $N^{15}NH^+$, i.e. H3c3 and H5c3.

3.1.4 Derivation of the total column densities

The complexity of the N_2H^+(1–0) line profiles, clearly seen in the spectra of Figs A-1–A-4, and described in Section 3.1.3, makes it difficult to obtain fits with low residuals. Therefore, we have estimated the N_2H^+ total column density, $N_{tot}(N_2H^+)$, from the integrated intensity of the hyperfine component $F_1 = 0 - 1$, which is well separated in velocity from the others and intrinsically the faintest one, and hence potentially the least affected by optical depth effects, self-absorption, or contribution of secondary faint velocity features. This was then converted to the total integrated intensity of the line by multiplying it by 9, which is the relative strength of the sum of all components with respect to the $F_1 = 0 - 1$ one (see Table 2). Then, the total column density was calculated from the total integrated intensity using equation (A4) of Caselli et al. (2002), which assumes optically thin emission and same (and constant) excitation temperature, T_{ex}, for all rotational transitions (and all hyperfine components within each transition).

Obviously, this simplified approach provides column density estimates that need to be taken with caution, because the spectra of N_2H^+ in some cases show hints of multiple velocity features and/or self-absorption also in the $F_1 = 0 - 1$ component (see Figs A-1–A-4), as discussed in Section 3.1.3. In particular, when we could determine that the profile is due to multiple velocity features, we have integrated only the strongest velocity component, (e.g. the three cores in Cloud C, or D6c4, D5c5/6 and D8c1 in cloudD, see Section 3.1.3); when the line profile was attributed more likely to self-absorption (e.g. in the cores D6c6, D7c1 and D7c2), we have integrated the whole component, bearing in mind that this will provide a lower limit on $N_{tot}(N_2H^+)$, and hence a lower limit on the associated $^{14}N/^{15}N$ as well. In cores undetected in $N^{15}NH^+$, one cannot establish if the line profile of N_2H^+ is most likely due to multiple velocity components or to self-absorption, except in the cases in which velocity features well-separated in velocity are found (e.g. in H2c1 and H3c1). In the latter case, we have performed a fit assuming multiple velocity features, identified the strongest one (even in case of large residuals), and taken the integrated intensity of this velocity feature only.

Because the adopted approach does not allow to estimate the excitation temperature, T_{ex}, we have assumed a range of T_{ex} which can be considered typical or reasonable for IRDC cores, i.e. $\sim$10–50 K. This temperature range includes the dust temperature estimates obtained from Herschel for all clouds (see paper I), and the kinetic temperature estimates obtained in Cloud H ($\sim$10–20 K, Sokolov et al. 2017). The corresponding range of values for $N_{tot}(N_2H^+)$ is $\sim$0.8–14 $\times$ 10^{13} cm^{-2} at T_{ex} = 10 K, and $\sim$2.4–41 $\times$ 10^{14} cm^{-2} at T_{ex} = 50 K. The results are shown in Table 3.

For $N^{15}NH^+$, we have followed the same method as that used for the N_2H^+ lines: for the spectra in which the main hyperfine component only is detected, i.e. the F=2 − 1 one (see Table 2), we have estimated the total integrated intensity by dividing the integral of this component for its relative strength (i.e. $\sim$0.555, Table 2). The approach is appropriate for optically thin lines. We note that we cannot measure directly the optical depth of the lines because we detected the hyperfine structure only towards two cores, and even in these cases the measured τ is very uncertain (error on τ larger than τ). However, the assumption of optically thin lines is justified by the faint emission and the non-detection of the satellites, and supported by direct measurements in protostellar cores in which τ of $N^{15}NH^+$(1–0) is comparable to or smaller than $\sim$0.1 (e.g. towards OMC–2 FIR4, Fontani et al. 2020). As excitation temperature, we have used the same one assumed for N_2H^+.

We find $N_{tot}(N^{15}NH^+)$ in the range $\sim$1.3–7 $\times$ 10^{11} cm^{-2} at T_{ex} = 10 K, and $\sim$4–19 $\times$ 10^{11} cm^{-2} at T_{ex} = 50 K. We point out that even though the assumed temperature affects the column densities of N_2H^+ and $N^{15}NH^+$, it does not affect at all the $^{14}N/^{15}N$ ratio, as we will see in Section 4.1.

Finally, in the cores undetected in $N^{15}NH^+$, we have evaluated the upper limit on $N_{tot}(N^{15}NH^+)$ from the upper limit on the integrated intensity, estimated through

$$\int T_B dv = \frac{1}{0.555} 3\sigma \frac{\sqrt{\pi}}{2\sqrt{\ln 2}} \mathrm{FWHM}\ , \quad (2)$$

which expresses the integral in velocity of a Gaussian line with peak intensity given by the 3σ rms in the spectrum. The factor 0.555, which is the relative strength of the F = 2 − 1 hyperfine component,

Table 3. Total integrated line intensities ($\int T_B dv$) and total column densities (N_{tot}) of N_2H^+ and $N^{15}NH^+$ derived from the (1–0) transition as explained in Section 3, and their ratio $^{14}N/^{15}N$. For N_2H^+(1–0) the listed $\int T_B dv$ is obtained dividing the integrated intensity of the isolated hyperfine component (i.e. $F_1 = 0$–1, Col. 2) by 0.1111 (relative intensity of this component with respect to the total one). These integrated intensities are shown in Figs A-1–A-4. For lines with multiple velocity features also in the $F_1 = 0$–1 component and detected in $N^{15}NH^+$, we used the integrated intensity only of the feature corresponding in velocity to that of the $N^{15}NH^+$ line. For $N^{15}NH^+$ (1–0), we have computed $\int T_B dv$ from the integrated intensity of the main hyperfine component divided by 0.5555 (relative intensity of this component with respect to the total one) for all sources except for D5c5/6, F4c5, F4c7, for which all hyperfine components could be detected and integrated (column 5). The error on the line integral was computed according to the propagation of errors, and it is given by the expression $\sigma \times \Delta V \times \sqrt{n}$, where σ is the rms in the spectrum, ΔV the velocity resolution, and n the number of integrated channels. The errors on the column densities include the error on the line integrated intensity and the calibration uncertainty on the absolute flux density scale of 10 per cent. The quoted $^{14}N/^{15}N$ are derived from the column densities estimated assuming $T_{ex} = 10$ K, but those computed when using $T_{ex} = 50$ K are identical. The core names in the first column are taken from paper I, while in the last column we list the core ID number used in Fig. 1.

source	N_2H^+			$N^{15}NH^+$			$^{14}N/^{15}N$	ID
	$\int T_B dv$ (K km s^{-1})	N_{tot} ($\times 10^{13}$ cm^{-2}) T_{ex} = 10 K	N_{tot} ($\times 10^{13}$ cm^{-2}) T_{ex} = 50 K	$\int T_B dv$ (K km s^{-1})	N_{tot} ($\times 10^{11}$ cm^{-2}) T_{ex} = 10 K	N_{tot} ($\times 10^{11}$ cm^{-2}) T_{ex} = 50 K		
C1c1	13.8(0.2)	1.9(0.2)	5.4(0.6)	≤0.08	≤1.2	≤3.4	≥160	1
C1c2	11.2(0.1)	1.5(0.2)	4.4(0.5)	≤0.30	≤4.2	≤12.4	≥40	2
C1c3	21.4(0.3)	2.9(0.3)	8.4(1.0)	≤0.08	≤1.1	≤3.1	≥270	3
C2c1	25.2(0.2)	3.4(0.4)	9.9(1.1)	≤0.07	≤1.0	≤2.9	≥345	4
C2c2	42.6(0.2)	5.7(0.6)	16.7(1.8)	≤0.08	≤1.2	≤3.4	≥490	5
C2c3/5	37.6(0.3)	5.1(0.6)	14.8(1.6)	0.15(0.03)	2.1(0.7)	6(2)	240 ± 100	6
C2c4	46.7(0.3)	6.3(0.7)	18(2)	0.17(0.05)	2.4(0.9)	7(3)	260 ± 120	7
C2c6	34.8(0.2)	4.7(0.5)	13.7(1.5)	0.19(0.04)	2.6(0.9)	8(3)	180 ± 80	8
C5c3/4	17.2(0.2)	2.3(0.3)	6.8(0.7)	≤0.09	≤1.3	≤3.7	≥190	9
C5c1/2	21.1(0.3)	2.8(0.3)	8.3(0.9)	≤0.07	≤0.9	≤2.8	≥300	10
C6c5	16.9(0.3)	2.3(0.3)	6.7(0.8)	≤0.13	≤1.8	≤5.2	≥130	11
C6c6/8	20.7(0.4)	2.8(0.3)	8.1(1.0)	≤0.14	≤1.9	≤5.6	≥150	12
C6c1/2	19.0(0.3)	2.6(0.3)	7.5(0.9)	≤0.13	≤1.8	≤5.2	≥145	13
C6c7	19.0(0.5)	2.6(0.3)	7.5(0.9)	≤0.19	≤2.7	≤7.9	≥100	14
C6c9	9.5(0.5)	1.3(0.2)	3.8(0.6)	≤0.16	≤2.3	≤6.7	≥60	15
C6c10	15.7(0.7)	2.1(0.3)	6.2(0.9)	≤0.30	≤4.2	≤12.5	≥50	16
D3c3/4	8.1(0.3)	1.1(0.14)	3.2(0.4)	≤0.09	≤1.2	≤3.5	≥90	1
D3c5	6.8(0.2)	0.9(0.14)	2.7(0.3)	≤0.08	≤1.15	≤3.4	≥80	2
D6c1/2/3	20.3(0.2)	2.7(0.3)	8.0(0.9)	≤0.07	≤1.0	≤3.1	≥260	3
D6c4	18.8(0.3)	2.5(0.3)	7.4(0.9)	0.15(0.05)	2.0(0.9)	6(3)	120 ± 70	4
D6c5	29.2(0.4)	3.9(0.4)	11.5(1.3)	≤0.13	≤1.9	≤5.5	≥210	5
D5c7	26.4(0.4)	3.6(0.4)	10.4(1.2)	≤0.11	≤1.6	≤4.7	≥220	6
D6c6	24.0(0.5)	3.2(0.4)	9.5(1.1)	0.10(0.05)	1.4(0.8)	4(2)	230 ± 160	7
D7c1	21.2(0.2)	2.9(0.3)	8.4(0.9)	0.12(0.04)	1.7(0.7)	5(2)	170 ± 90	8
D7c2	21.6(0.2)	2.9(0.3)	8.5(0.9)	0.16(0.05)	2.2(0.9)	6(3)	130 ± 70	9
D5c7	14.2(0.2)	1.9(0.2)	5.6(0.6)	≤0.07	≤0.9	≤2.7	≥210	10
D5c5/6	16.6(0.1)	2.2(0.2)	6.5(0.7)	0.09(0.04)	1.3(0.7)	4(2)	170 ± 100	11
D7c3	17.2(0.3)	2.3(0.3)	6.8(0.8)	≤0.07	≤1.0	≤3.0	≥230	12
D8c1	28.9(0.1)	3.9(0.4)	11.4(1.2)	0.10(0.02)	1.4(0.4)	4.0(1.3)	280 ± 120	13
D5c3	27.0(0.2)	3.6(0.4)	10.6(1.2)	≤0.06	≤0.9	≤2.6	≥400	14
D5c1	19.3(0.2)	2.6(0.3)	7.6(0.8)	≤0.06	≤0.9	≤2.6	≥290	15
D9c1/2	21.8(0.6)	2.9(0.4)	8.6(1.1)	≤0.17	≤2.4	≤7.1	≥120	16
F1c1	104.2(0.3)	14.0(1.4)	41(4)	0.26(0.03)	3.6(0.8)	11(2)	390 ± 130	1
F1c2	89.6(0.5)	12.1(1.3)	35(4)	0.21(0.06)	3.0(1.1)	9(3)	400 ± 190	2
F1c3	74.7(0.5)	10.1(1.1)	29(3)	0.47(0.09)	7(2)	19(6)	150 ± 60	3
F1c4	39.8(0.2)	5.4(0.6)	15.7(1.6)	0.14(0.04)	2.0(0.8)	6(2)	270 ± 140	4
F1c5	6.1(0.3)	0.8(0.12)	2.4(0.4)	≤0.13	≤1.8	≤5.2	≥50	5
F1c6	14.6(0.2)	2.0(0.2)	5.7(0.7)	≤0.08	≤1.1	≤3.1	≥190	6
F2c1	17.7(0.2)	2.4(0.3)	7.0(0.8)	≤0.06	≤0.8	≤2.4	≥290	7
F3c1/2	17.4(0.1)	2.3(0.3)	6.8(0.7)	≤0.06	≤0.8	≤2.5	≥280	8
F3c3	13.4(0.3)	1.8(0.2)	5.3(0.6)	≤0.09	≤1.3	≤3.7	≥140	9
F3c4	14.1(0.2)	1.9(0.2)	5.6(0.6)	≤0.07	≤1.0	≤2.9	≥190	10
F4c4	18.2(0.2)	2.5(0.3)	7.2(0.8)	≤0.08	≤1.1	≤3.3	≥220	11
F4c5	25.8(0.2)	3.5(0.4)	10.2(1.1)	0.14(0.05)	2.0(0.8)	6(2)	175 ± 90	12
F4c6	29.1(0.3)	3.9(0.4)	11.4(1.3)	≤0.11	≤1.5	≤4.4	≥260	13
F4c7	52.8(0.3)	7.1(0.8)	21(2)	0.27(0.7)	3.8(1.4)	11(4)	190 ± 90	14
F4c8	55.3(0.3)	7.4(0.8)	22(2)	≤0.11	≤1.6	≤4.6	≥470	15
F4c9	35.0(0.3)	4.7(0.5)	13.8(1.5)	≤0.11	≤1.6	≤4.6	≥300	16

Table 3 – *continued*

source	N_2H^+			$N^{15}NH^+$			$^{14}N/^{15}N$	ID
	$\int T_B dv$ (K km s^{-1})	N_{tot} ($\times 10^{13}$ cm^{-2}) T_{ex} = 10 K	N_{tot} ($\times 10^{13}$ cm^{-2}) T_{ex} = 50 K	$\int T_B dv$ (K km s^{-1})	N_{tot} ($\times 10^{11}$ cm^{-2}) T_{ex} = 10 K	N_{tot} ($\times 10^{11}$ cm^{-2}) T_{ex} = 50 K		
F4c10	17.6(0.4)	2.4(0.3)	6.9(0.8)	≤0.11	≤1.5	≤4.5	≥160	17
F4c1	13.0(0.2)	1.7(0.2)	5.1(0.6)	≤0.14	≤2.0	≤5.9	≥90	18
F2c2	8.0(0.2)	1.1(0.13)	3.2(0.4)	≤0.09	≤1.3	≤3.8	≥84	19
F3c5	19.4(0.3)	2.6(0.3)	7.6(0.8)	≤0.09	≤1.3	≤3.8	≥200	20
H3c4	15.4(0.2)	2.1(0.2)	6.1(0.7)	≤0.10	≤1.3	≤3.9	≥160	1
H3c5	12.6(0.3)	1.7(0.2)	5.0(0.6)	≤0.16	≤2.3	≤6.6	≥75	2
H3c6	8.6(0.3)	1.2(0.15)	3.4(0.4)	≤0.17	≤2.4	≤7.1	≥50	3
H3c3	20.7(0.3)	2.8(0.3)	8.1(0.9)	0.12(0.03)	1.7(0.6)	5.1(1.8)	160 ± 70	4
H2c1	13.6(0.3)	1.8(0.2)	5.3(0.6)	≤0.14	≤2.0	≤5.8	≥90	5
H3c2	24.0(0.2)	3.2(0.4)	9.5(1.0)	≤0.11	≤1.6	≤4.6	≥200	6
H4c1	21.3(0.2)	2.9(0.3)	8.4(0.9)	≤0.14	≤1.9	≤5.7	≥150	7
H3c1	17.2(0.3)	2.3(0.3)	6.8(0.7)	≤0.14	≤2.0	≤5.8	≥120	8
H5c3	26.1(0.2)	3.5(0.4)	10.3(1.1)	0.31(0.06)	4.3(1.3)	13(4)	80 ± 30	9
H5c1	18.1(0.3)	2.4(0.3)	7.1(0.8)	≤0.15	≤2.1	≤6.1	≥120	10

is introduced to convert the upper limit of this component to the upper limit of the total one. The assumed FWHM is the mean value measured from the $N^{15}NH^+$ lines detected in each cloud.

The N_2H^+ and $N^{15}NH^+$ column densities have been calculated assuming that N_2H^+ and $N^{15}NH^+$ (1–0) have the same T_{ex} based on the assumption that the two transitions have very similar critical densities, and hence similar excitation conditions. However, let us discuss this assumption better. Based on a non-LTE analysis, Hily-Blant et al. (2013a) found differences in T_{ex} for lines with the same quantum numbers of the different isotopologues of HCN. But these differences are in all (but one) cases below $\sim$ 10 per cent, indicating that a significantly different T_{ex} for lines with the same quantum numbers is unlikely for isotopologues of the same species. Regarding the possibility that different hyperfine components of the same isotopologue can have a different T_{ex}, (Daniel, Cernicharo & Dubernet 2006) showed that high optical depths in N_2H^+ (1–0) could indeed cause deviations from the line profile expected when each component has the same excitation temperature. However, both theoretical (Daniel et al. 2006) and observational (Caselli et al. 1995) works show that T_{ex} of the component analysed in our work, i.e. the $F_1 = 0 - 1$ one, would deviate from the local thermodynamic equilibrium value by 10-15 per cent at most even in the high optical depth case, and only at H_2 volume densities below 10^5 cm^{-3} (see fig. 6 in Daniel et al. 2006). In our cores, the average H_2 volume density is $n_{H_2} = 7.6^{+5.2}_{-2.6} \times 10^5$ cm^3, or when using the background subtracted mass $n^b_{H_2} = 3.4^{+2.4}_{-1.8} \times 10^5$ cm^3 (paper I), for which the predicted deviations from the equilibrium T_{ex} is negligible (fig. 6 in Daniel et al. 2006). Therefore we are confident that hyperfine anomalies are not affecting significantly the T_{ex} of the analysed component.

3.2 Spectra towards the N_2H^+ cores

For completeness, we have extracted and analysed the spectra associated with the cores identified through the N_2H^+ emission. These spectra, shown in Figs. A-5–A-8, were obtained with the dendrogram analysis like the 3 mm continuum cores in paper I. The extraction regions are shown in Fig. 1, labelled following a method similar to the one used in paper I for the continuum cores: we identify the closer core in Butler & Tan (2012), to which we add the label 'n2hp', followed by a sequential number in case more than one core can be associated with the same Butler & Tan (2012) core. Most of these cores are more extended than the continuum ones, which are included in the N_2H^+ contours especially in clouds C, D, and H. Therefore, this analysis allows us to investigate if the $N^{15}NH^+$ emission is more extended, or, to say it in another way, 'detectable' also away from the continuum cores. The method adopted to extract the spectra from these cores, convert them from flux density to T_B unit, fit them, and derive the column densities, are identical to those described in Section 3.1.

In Fig. 1 we highlight the cores in which $N^{15}NH^+$ has been detected with signal-to-noise ratio ≥3. In Cloud C, the two detected cores, C2-n2hp-1 and C2-n2hp-2, include the continuum cores already detected in $N^{15}NH^+$, i.e. C2c3/5, C2c4, and C2c6; therefore, we have not found 'new' detections. The same result is found in Cloud F, in which again $N^{15}NH^+$(1–0) is detected only towards the two cores (F1-n2hp-1 and F4-n2hp-1) that include in their contours all the continuum cores already detected in this line. In Cloud D, we have detected $N^{15}NH^+$ towards D5-n2hp-1 and D7-n2hp-1: D7-n2hp-1 includes the already detected continuum core D8c1, while D5-n2hp-1 contains the undetected continuum core D5c7, but D5-n2hp-1 is much more extended than D5c7. Hence, in this case the $N^{15}NH^+$ emission arises from the diffuse envelope of D5c7. Apart from this case, overall in clouds C, D, and F the detections in the continuum and N_2H^+ cores are always consistent.

The case of Cloud H is more complicated. In this cloud we detect $N^{15}NH^+$ towards two cores: H2-n2hp-1, which includes the much more compact undetected continuum cores H2c1 and H3c1, and H5-n2hp-1, which includes the continuum core H5c3, detected in $N^{15}NH^+$. Hence, the detection in H2-n2hp-1 is due to emission in the extended envelopes of H2c1 and H3c1, as in D5-n2hp-1. There is also a peculiar case: H3-n2hp-2, which is undetected in $N^{15}NH^+$ but includes the compact continuum core H3c3 detected in $N^{15}NH^+$. Therefore, the non-detection in H3-n2hp-2 appears inconsistent at first glance with the detection towards H3c3. In this latter, $N^{15}NH^+$ (1–0) is displaced by $\sim$1.8 km s^{-1} from the systemic velocity of the cloud (see Fig. 3). This detection could hence be doubtful. However, a displacement of about 1 km s^{-1} is seen also in the N_2H^+ (1–0) line (see Fig. A-4). Furthermore, and most importantly, the noise in the H3-n2hp-2 spectrum is about 5 times higher than that in the H3c3 one (see Fig. 3), and the hint of a possible line under the noise level is apparent in H3-n2hp-2 as well. Therefore, we conclude that the detection of $N^{15}NH^+$ towards H3c3, detected with signal to noise of 5, is real.

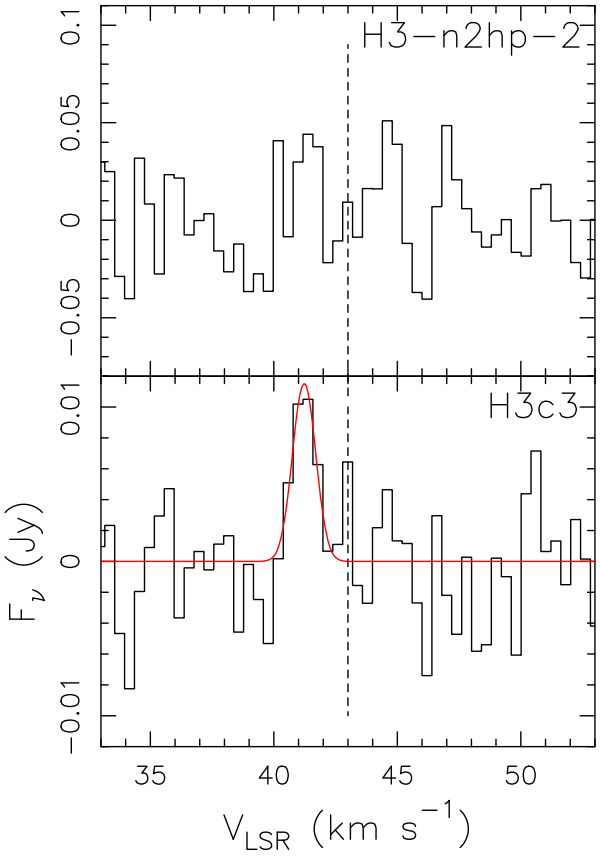

Figure 3. Comparison between the spectra of $N^{15}NH^+$(1–0) extracted in flux density units of cores H–d (top) and H3c3 (bottom). H3c3 is included in H3-n2hp-2, but the higher rms noise in H–d prevents the detection of $N^{15}NH^+$ (1–0) at about 41.2 km s^{-1} towards H3c3. The dashed vertical line indicates the systemic velocity of Cloud H of 43 km s^{-1}.

In summary, $N^{15}NH^+$ (1–0) has been detected towards N_2H^+ cores not previously detected in continuum cores only in two sources, D5-n2hp-1 and H2-n2hp-1. This result suggests that, overall, the $N^{15}NH^+$ emission seems to be fainter in the more diffuse N_2H^+ cores than in the compact continuum cores. We will discuss further this finding in Sections 4.1 and 4.2.

The N_2H^+ and $N^{15}NH^+$ column densities have been computed adopting the same approach described in Section 3.1.4. Among the cores that show complex line profiles in N_2H^+(1–0), D7-n2hp-1 is the only one in which the profile can be attributed to self-absorption based on the comparison between the velocity peak of $N^{15}NH^+$ and the $F_1 = 0 - 1$ hyperfine component of N_2H^+. The results are shown in Table 4. For N_2H^+, we find N_{tot} in the range 0.55–5.5 $\times$ 10^{13} cm^{-2} when T_{ex} is $\sim$10 K, and 1.6–16.1 $\times$ 10^{13} cm^{-2} when T_{ex} is $\sim$50 K. For $N^{15}NH^+$, we find N_{tot} in the range 0.8–3.3 $\times$ 10^{11} cm^{-2} when T_{ex} is $\sim$10 K, and 2.3–9.6 $\times$ 10^{11} cm^{-2} when T_{ex} is $\sim$50 K. In Table 4 we also list the N_2D^+ cores identified in Kong et al. (2017) which can be associated with the N_2H^+ cores. A few of them are indeed associated, but unfortunately only 4 of those are also detected in $N^{15}NH^+$, and thus the statistics is too low to discuss possible relations between nitrogen and deuterium fractionation.

4 DISCUSSION

4.1 $^{14}N/^{15}N$ ratios in the continuum cores

In Fig. 4 we plot $N_{tot}(N^{15}NH^+)$ against $N_{tot}(N_2H^+)$ computed for the continuum cores. Their ratios, $^{14}N/^{15}N$ (shown in Table 3), are in between $\sim$80 and $\sim$400, with little statistically significant differences among the clouds: the average $^{14}N/^{15}N$ is 230 $\pm$ 50 for Cloud C, 180 $\pm$ 100 for Cloud D, 260 $\pm$ 100 for Cloud F, and 120 $\pm$ 40 for Cloud H. The cores have also been divided in Fig. 4 in two groups: starless or star-forming, based on the absence or presence, respectively, of an embedded infrared emission. This classification was made in paper I, and we will discuss the $^{14}N/^{15}N$ in the two groups in Section 4.3.

Inspection of Fig. 4 indicates:

(1) a variability in the $^{14}N/^{15}N$ ratio of a factor $\sim$4, smaller than the factor $\sim$10 found in other IRDCs and high-mass star-forming regions at lower angular resolution by Zeng et al. (2017) and Fontani et al. (2015), but similar to that measured in HCN and HNC by Colzi et al. (2018b);

(2) an average $^{14}N/^{15}N$ of $\sim$210, very similar to the terrestrial one (Marty, Zimmermann & Burnard 2009). Assuming Galactocentric distances for the four clouds in between $\sim$4.6 and $\sim$6.3 kpc (Zeng et al. 2017), the present-day $^{14}N/^{15}N$ ratio of the ISM at the Galactocentric distance of the sources is $\sim$300–330, estimated from the trend derived by Colzi et al. (2019, see their equations 5 and 6) from HCN and HNC isotopologues. Hence, the average $^{14}N/^{15}N$ ratio measured in this work is $\sim$1.5 times smaller than the ISM value at the Galactocentric distance of the sources;

(3) in two cores, i.e. D6c4 and H5c3, we measure $^{14}N/^{15}N$ ratios around 100, i.e. lower by a factor $\sim$3 with respect to the local ISM value, and comparable to (or slightly smaller than) the cometary values.

In Fig. 4 we highlight the difference with the single-dish survey of Fontani et al. (2015), in which the measured range of $^{14}N/^{15}N$ from N_2H^+ isotopologues is $\sim$180–1300, namely twice wider than ours and hence with a higher average value. A wider range in $^{14}N/^{15}N$ was also measured in HCN and HNC towards the IRDC cores studied by Zeng et al. (2017) with a single-dish. Also, the two cores D6c4 and H5c3 have among the lowest $^{14}N/^{15}N$ ratios ever measured in N_2H^+, and similar to the values obtained by Colzi et al. (2019) towards IRAS 05358 + 3543. This would indicate that the smaller spatial scales probed by the ALMA interferometer can identify spots with lower $^{14}N/^{15}N$ values much better than single-dish observations can.

To investigate more in detail the influence of the diffuse gas surrounding the dense cores on the measured $^{14}N/^{15}N$, we have derived the $^{14}N/^{15}N$ ratios towards the cores detected in $N^{15}NH^+$ from the total power data only. We have extracted and analysed the total power spectra following the same approach described in Sections 3.1.1 and 3.1.4. The only difference is that in equation (1) we used the telescope FWHM to convert from flux density to main beam temperature units. The half-power beamwidth of the total power data is $\sim$70 arcsec for both $N^{15}NH^+$ and N_2H^+ (1–0), so that the spectra extracted from one position can contain the contribution of nearby cores. Therefore, in case of cores separated by less than half of the beamwidth, i.e. $\sim$35 arcsec, we have extracted only one single-dish spectrum. The results are shown in Table 5. In all cores except F1c1, which is the most extended one, the beam-averaged $^{14}N/^{15}N$ ratios are larger by a factor $\sim$1.5–3 than those obtained in the embedded cores at higher angular resolution. This result strengthens our conclusion that in the diffuse envelope of the cores the isotopic

Table 4. Same as Table 3 for the N_2H^+ cores (Fig. 1). The ID letters in column 10 are used to identify the cores in Fig. 1. In column 11 we list if the core can be associated with one of the N_2D^+ cores identified in Kong et al. (2017). For $N_{tot}(N^{15}NH^+)$, we used the area obtained from the Gaussian fit to the main hyperfine component for all sources except for C–b and F–l, for which we used the total integrated intensity of all hyperfine components detected.

Source	N_2H^+			$N^{15}NH^+$			$^{14}N/^{15}N^a$	ID	N_2D^+
	$\int T_B dv$ (K km s^{-1})	N_{tot} ($\times 10^{13}$ cm^{-2}) $T_{ex}=10$ K	N_{tot} ($\times 10^{13}$ cm^{-2}) $T_{ex}=50$ K	$\int T_B dv$ (K km s^{-1})	N_{tot} ($\times 10^{11}$ cm^{-2}) $T_{ex}=10$ K	N_{tot} ($\times 10^{11}$ cm^{-2}) $T_{ex}=50$ K			
C1-n2hp-1	1.8(0.1)	2.2(0.3)	6.4(1.0)	≤0.03	≤0.8	≤2.2	≥290	a	C1N
C2-n2hp-1	4.36(0.02)	5.3(0.6)	15.0(1.6)	0.10(0.03)	1.5(0.6)	4.5(1.7)	350(190)	b	C2C
C2-n2hp-2	3.87(0.02)	4.7(0.5)	13.7(1.4)	0.10(0.02)	2.5(0.8)	7(2)	190(80)	c	C2A/B
C5-n2hp-1	1.61(0.01)	2.0(0.2)	5.7(0.6)	≤0.04	≤1.0	≤3.0	≥194	d	C5A
C6-n2hp-1	1.82(0.02)	2.2(0.3)	6.4(0.7)	≤0.07	≤1.8	≤5.2	≥125	e	
D3-n2hp-1	1.14(0.01)	1.4(0.2)	4.0(0.4)	≤0.05	≤1.3	≤3.7	≥110	a	
D6-n2hp-1	1.10(0.01)	1.3(0.2)	3.9(0.4)	≤0.05	≤1.3	≤3.7	≥106	b	
D5-n2hp-1	1.33(0.01)	1.6(0.2)	4.0(0.4)	0.05(0.01)	1.3(0.4)	3.7(1.1)	130(60)	c	
D5-n2hp-2	1.17(0.01)	1.4(0.2)	4.1(0.5)	≤0.07	≤1.8	≤5.2	≥80	d	
D7-n2hp-1	3.05(0.02)	3.7(0.4)	10.8(1.2)	0.05(0.01)	1.3(0.4)	3.7(1.1)	290(120)	e	
D5-n2hp-3	1.74(0.02)	2.1(0.3)	6.2(0.7)	≤0.07	≤1.8	≤5.2	≥120	f	
D9-n2hp-1	0.86(0.01)	1.0(0.1)	3.0(0.3)	≤0.05	≤1.3	≤3.7	≥83	g	
F1-n2hp-1	4.55(0.01)	5.5(0.6)	16.1(1.6)	0.13(0.01)	3.3(0.6)	9.6(1.7)	170(50)	a	
F1-n2hp-2	0.45(0.01)	0.55(0.07)	1.6(0.2)	≤0.05	≤1.3	≤3.7	≥43	b	F1
F1-n2hp-3	0.54(0.01)	0.65(0.08)	1.9(0.2)	≤0.07	≤1.8	≤5.2	≥37	c	
F1-n2hp-4	1.07(0.01)	1.3(0.2)	3.8(0.4)	≤0.06	≤1.5	≤4.4	≥86	d	
F1-n2hp-5	0.80(0.01)	1.0(0.1)	2.8(0.3)	≤0.05	≤1.3	≤3.7	≥77	e	
F2-n2hp-1	0.60(0.01)	0.73(0.08)	2.1(0.3)	≤0.07	≤1.8	≤5.2	≥41	f	
F2-n2hp-2	1.26(0.01)	1.5(0.2)	4.5(0.5)	≤0.04	≤1.0	≤3.0	≥152	g	F2
F2-n2hp-3	0.93(0.02)	1.1(0.2)	3.3(0.4)	≤0.07	≤1.8	≤5.2	≥64	h	
F3-n2hp-1	1.88(0.01)	2.3(0.3)	6.7(0.7)	≤0.04	≤1.0	≤3.0	≥227	i	
F4-n2hp-1	2.52(0.01)	3.1(0.4)	8.9(0.9)	0.056(0.008)	0.8(0.2)	2.3(0.6)	390(140)	l	
F4-n2hp-2	0.48(0.01)	0.58(0.07)	1.7(0.2)	≤0.06	≤1.5	≤4.4	≥39	m	
F4-n2hp-3	0.98(0.02)	1.2(0.2)	3.5(0.4)	≤0.04	≤1.0	≤3.0	≥120	n	
H1-n2hp-1	1.04(0.01)	1.3(0.2)	3.7(0.4)	≤0.03	≤0.8	≤2.2	≥167	a	
H1-n2hp-2	1.61(0.01)	2.0(0.2)	5.7(0.6)	≤0.03	≤0.8	≤2.2	≥260	b	H1A
H3-n2hp-1	1.24(0.01)	1.5(0.2)	4.4(0.5)	≤0.02	≤0.5	≤1.5	≥300	c	
H3-n2hp-2	1.04(0.01)	1.3(0.2)	3.7(0.4)	≤0.02	≤0.5	≤1.5	≥251	d	H3A
H2-n2hp-1	1.43(0.01)	1.7(0.2)	5.1(0.6)	0.027(0.008)	0.7(0.3)	2.0(0.8)	260(130)	e	H2A/B/C/D/E/G
H5-n2hp-1	1.41(0.01)	1.7(0.2)	5.0(0.5)	0.05(0.012)	1.3(0.4)	3.7(1.3)	140(60)	f	H5A

[a]Derived from the column densities estimated assuming $T_{ex}=10$ K, but the ratios are identical when using $T_{ex}=50$ K.

ratio tends to be larger, as predicted by the selective photodissociation scenario, and also stresses the need for high-angular resolution data to derive correct values of the $^{14}N/^{15}N$ ratio and accurately measure the ^{15}N fractionation in the cores embedded within the IRDC.

However, as one can see in Fig. 4, all lower limits on $^{14}N/^{15}N$ are below ∼400, and the maximum measured $^{14}N/^{15}N$ ratios are ∼390 and ∼400 towards F1c1 and F2c2, respectively. This means that our interferometric observations are not sensitive to $N^{15}NH^+$ emission in cores with $^{14}N/^{15}N$ higher than ∼400, and hence we cannot conclude if the narrower range of isotopic ratios measured in this work depends also on our limited sensitivity. Another caveat on the $^{14}N/^{15}N$ ratios arises from the possible non-negligible optical depth of the $F_1=0-1$ component of $N_2H^+(1–0)$, which could lead us to underestimate $N_{tot}(N_2H^+)$ and, from this, the $^{14}N/^{15}N$ ratio. This comment applies especially to core H5c3, which has the lowest $^{14}N/^{15}N$ ratio (∼80). The fit to the hyperfine structure of this line provides an optical depth of the main component $\tau\sim8$, and hence τ of the $F_1=0-1$ component would be ∼0.89 (Fig. A-4). This would introduce a correction $\tau/(1-\exp(-\tau))\sim1.7$ in the N_2H^+ column density, and hence the $^{14}N/^{15}N$ would become ∼140, still about a factor 2 smaller than the ISM value at the Galactocentric distance of the source.

4.2 $^{14}N/^{15}N$ ratios in the N_2H^+ cores

Let us now analyse the $^{14}N/^{15}N$ ratio towards the N_2H^+ cores. The N_2H^+ and $N^{15}NH^+$ column densities are listed in Table 4, and shown in Fig. 5: the range of $^{14}N/^{15}N$ is ∼130–390, consistent with the one found in the continuum cores (compare Figs 4 and 5). For the N_2H^+ cores encompassing continuum cores, all $^{14}N/^{15}N$ are consistent among them within the uncertainties, or slightly higher (about a factor ∼1.5–2, like in C–b, F–l and H–f), which indicates that the $^{14}N/^{15}N$ ratio in the core envelopes is either similar to or higher than that measured in their embedded dense continuum cores.

Overall, the non-detection of $N^{15}NH^+$ in N_2H^+ cores without continuum cores, and the fact that the $^{14}N/^{15}N$ ratios in the N_2H^+ cores is (almost) never smaller than the values measured in their embedded 3 mm continuum cores suggests that the $^{14}N/^{15}N$ ratio tends to be higher in the more extended and diffuse gas. This result is in agreement with the high-angular resolution study of Colzi et al. (2019) towards the high-mass protocluster IRAS 05358 + 3543: in this source, the authors show that in the individual star-forming cores the $^{14}N/^{15}N$ ratio is lower by a factor two than in the extended, diffuse envelope. Colzi et al. (2019) concluded that this could be due to selective photodissociation (Heays et al. 2014, Lee et al. 2021). This mechanism would act like this: because UV photons cause

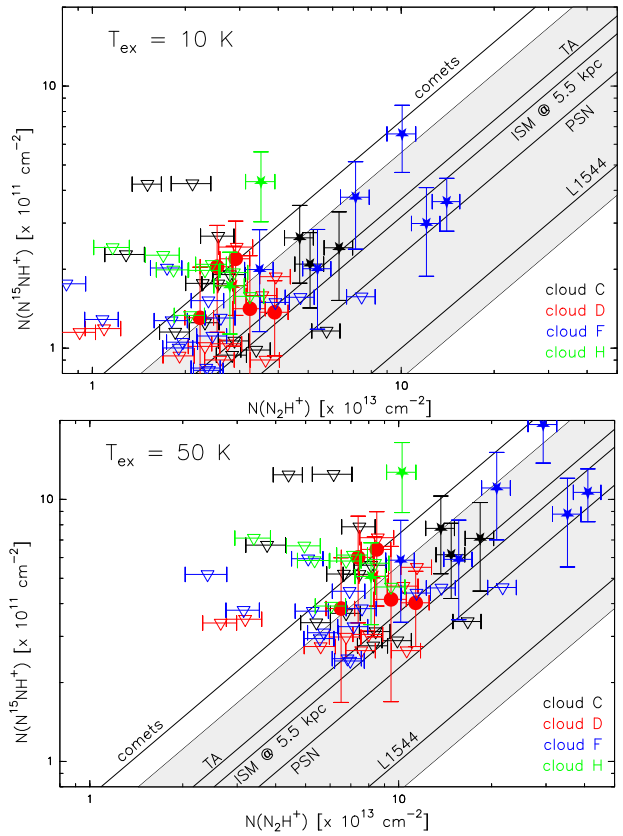

Figure 4. Column density of N_2H^+ against that of $N^{15}NH^+$ assuming T_{ex} = 10 K (top panel) and T_{ex} = 50 K (bottom panel). The values refer to the spectra extracted from the continuum cores (see Fig. 1). In both panels, the filled symbols represent the sources detected in $N^{15}NH^+$, and the open triangles correspond to the upper limits on $N(N^{15}NH^+)$. Among the detected sources, stars indicate cores with signs of star formation (in the form of embedded infrared sources), while circles correspond to cores without protostellar activity. The colours indicate the cores extracted from the different clouds as labelled in the bottom left corner. The solid lines indicate the mean $^{14}N/^{15}N$ composition as measured in: comets (∼136, Shinnaka et al. 2016); the terrestrial atmosphere (TA; ∼270, Marty et al. 2009); the ISM at the average Galactocentric distance of the sources of 5.5 kpc (∼316, average value derived from the trends of Colzi et al. 2018b); the protosolar nebula (PSN, ∼441; Marty et al. 2010); the pre-stellar core L1544 (∼1000; Bizzocchi et al. 2013). The grey band indicates the range of $^{14}N/^{15}N$ measured by Fontani et al. (2015) in a sample of high-mass star-forming cores with the IRAM-30m telescope.

photodissociation of $^{14}N^{15}N$, the progenitor of $N^{15}NH^+$, but not of the self-shielded $^{14}N_2$, the progenitor of N_2H^+, one would expect a decrease of the $N^{15}NH^+$ abundance with respect to N_2H^+ in the external layers exposed to external interstellar UV photons (and hence an increase of the $^{14}N/^{15}N$ ratio). However, care needs to be taken in this interpretation because most upper limits are comparable to the measured $^{14}N/^{15}N$ in the detected cores, and hence to show that the $^{14}N/^{15}N$ ratio is higher in the external, more diffuse part of the dense cores, higher sensitivity measurements of the $N^{15}NH^+$ column densities are needed.

An interesting exception is F1-n2hp-1: its $^{14}N/^{15}N$ ratio is 170 ± 50, while those of the four 3 mm continuum cores embedded in it vary from ∼390 to ∼150. Only F1c3 has a $^{14}N/^{15}N$ very similar to that of F1-n2hp-1 (150 against 170, respectively), while the others, F1c1, F1c2, and F1c4, have ratios higher by a factor ∼1.5–2. Hence, in these cases the $^{14}N/^{15}N$ ratio associated with the diffuse envelope of the continuum cores has a lower $^{14}N/^{15}N$, at odds with selective photodissociation if the UV photons are produced by an external field. A possible explanation still consistent with the selective photodissociation scenario is that internal UV photons are produced by the protostar(s) embedded in F1c1 instead of by an external UV field, and hence in this case the $N^{15}NH^+$ abundance is expected to be lower (and hence the $^{14}N/^{15}N$ ratio to be higher) in the dense protostellar core than in the envelope. Also, F1-n2hp-1 is very extended (Fig. 1) and in principle can include gas not only associated with the external envelope of F1c1, F2c2, F2c3, and F2c4, but also with other gaseous components having possibly different (and unknown) physical properties.

4.3 Relation between $^{14}N/^{15}N$ and star-formation activity

As stated in Section 4.1, in paper I the 3 mm continuum cores have been classified as starless or star-forming based on the absence or presence, respectively, of infrared emission. We can check if the measured $^{14}N/^{15}N$ ratios changes with the presence/absence of star-formation activity within the cores. In Fig. 4, we indicate with different symbols the starless and star-forming cores. Among the 13 detections, we find five starless and 12 star-forming cores, respectively. The average $^{14}N/^{15}N$ ratio is slightly lower (∼190) in the starless cores than in the protostellar objects (∼220). However, given the large dispersions, we confirm overall the result suggested by previous works (Fontani et al. 2015; Zeng et al. 2017; Colzi et al. 2018a,b): time does not seem to play a role in the enrichment, or depletion, of ^{15}N in N_2H^+.

Interestingly, the $^{14}N/^{15}N$ ratio in starless cores seems slightly lower on average than the values typically measured towards well known pre-stellar cores (e.g. by Bizzocchi et al. 2013; Redaelli et al. 2018). However, again care needs to be taken in the interpretation of this result. In fact, first the nature of our starless cores could not be 'pre–stellar' but just starless or star-forming in a very early stage of star-formation activity; second, some cores are extended and could contain smaller fragments in different evolutionary stages. For example, a core considered as starless could encompass smaller fragments already star-forming undetected in the IR images (see e.g. Liu et al. 2018). Therefore, in summary the results confirm the previous claim that evolution does not seem to play a role in the fractionation of nitrogen, but observations at higher sensitivity and angular resolution are needed to confirm or deny this conclusion.

4.4 Relation between $^{14}N/^{15}N$ and core properties

In Figs 6 and 7, we compare the $^{14}N/^{15}N$ ratios in the 17 continuum cores detected in $N^{15}NH^+$ with some physical properties that were derived in paper I and are listed in Table 6, namely: radius (R_{eff}), gas mass (M), dust temperature (T_{dust}, used to compute M), sonic Mach number ($\mathcal{M}_S$), virial parameter (α_{vir}), H_2 volume density ($n(H_2)$), and H_2 column density ($N(H_2)$). This latter was derived in three ways: from the Herschel data ($N(H_2)^{Her}$), from the 3 mm continuum mean flux density ($N(H_2)^{mean}$) and from the 3 mm continuum peak flux density ($N(H_2)^{peak}$). For quantities that in paper I have been derived from background subtracted and non-subtracted data, such as the mass and the H_2 volume density, we have adopted the non-subtracted data. The parameters derived from the Herschel maps (i.e. T_{dust} and $N(H_2)^{Her}$) were obtained by resampling the Herschel maps to the higher resolution of the ALMA data via a bilinear interpolation. The methods used to derive each parameter are described in paper I.

Table 5. Integrated line intensities ($\int T_{MB}dv$), total column densities (N_{tot}) of N_2H^+ and $N^{15}NH^+$, and their ratio $^{14}N/^{15}N$, obtained from the spectra extracted from the total power data only. The central position of the extracted spectra is the core listed in column 1 (see Section 3), and the extraction region corresponds to the total power beamwidth at half-maximum (∼70 arcsec). For N_2H^+(1–0), the listed $\int T_{MB}dv$ is that of the $F_1 = 0$–1 hyperfine component only, which has a relative intensity of 0.111 with respect to the total one. For $N^{15}NH^+$(1–0) the listed $\int T_{MB}dv$ is that of the F = 2–1 hyperfine component only, which has a relative intensity of 0.555 with respect to the total one.

Source	N_2H^+			$N^{15}NH^+$			$^{14}N/^{15}N$
	$\int T_{MB}dv$ (K km s^{-1})	N_{tot} (× 10^{13} cm^{-2}) T_{ex} = 10 K	N_{tot} (× 10^{13} cm^{-2}) T_{ex} = 50 K	$\int T_{MB}dv$ (K km s^{-1})	N_{tot} (× 10^{11} cm^{-2}) T_{ex} = 10 K	N_{tot} (× 10^{11} cm^{-2}) T_{ex} = 50 K	
C2c4	34.5(0.2)	4.2(0.4)	12.2(1.3)	0.33(0.03)	8.3(1.6)	24(5)	500(150)
D6c4	26.7(0.2)	3.2(0.3)	9.5(1.0)	0.35(0.03)	8.8(1.6)	26(5)	370(100)
D8c1	30.5(0.2)	3.7(0.4)	10.8(1.2)	0.45(0.05)	11(2)	33(7)	330(100)
F1c1	67.9(0.2)	8.2(0.8)	24(3)	0.78(0.09)	20(4)	60(12)	420(130)
F4c7	21.8(0.2)	2.6(0.3)	7.7(0.8)	0.27(0.04)	6.8(1.7)	20(5)	390(140)
H3c3	16.8(0.2)	2.0(0.2)	6.0(0.7)	0.28(0.04)	7.0(1.7)	21(5)	290(100)
H5c3	14.0(0.2)	1.7(0.2)	5.0(0.6)	0.24(0.04)	6.0(1.6)	18(5)	280(100)

Table 6. Core properties derived in paper I: radius (R_{eff}), mass (M), dust temperature (T_{dust}, used to compute M), sonic Mach number ($\mathcal{M}_S$), virial parameter (α_{vir}), H_2 volume density ($n(H_2)$), and H_2 column density derived in three ways: from the Herschel data ($N(H_2)^{Her}$), from the 3 mm mean continuum flux density ($N(H_2)^{mean}$), and from the 3 mm peak flux density ($N(H_2)^{peak}$). M, α_{vir}, $n(H_2)$, and $N(H_2)$ were calculated from the background subtracted 3 mm flux densities.

Core	$^{14}N/^{15}N$[a]	R_{eff} (pc)	M ($M_\odot$)	T_{dust} (K)	$\mathcal{M}_S$	α_{vir}	$n(H_2)$ (× 10^5 cm^{-3})	$N(H_2)^{Her}$	$N(H_2)^{mean}$ (× 10^{23} cm^{-2})	$N(H_2)^{peak}$
Starless cores										
D6c4	120	0.069	49	16	1.9	0.41	5.28	0.78	1.06	1.98
D6c6	230	0.048	20	16	2.7	1.18	6.29	0.89	0.88	1.11
D7c2	130	0.068	41	16	1.8	0.43	4.48	1.06	0.89	1.06
D5c5/6	170	0.161	247	15	3.8	0.60	2.06	1.18	0.97	2.17
D8c1	280	0.123	259	16	1.9	0.14	4.83	1.12	1.73	6.08
Star-forming cores										
C2c3/5	240	0.057	75	17	2.4	0.34	14.3	0.89	2.36	3.46
C2c4	260	0.048	53	17	3.3	0.71	16.6	0.91	2.32	3.23
C2c6	180	0.063	77	17	2.7	0.44	10.8	0.76	1.98	3.44
D7c1	170	0.078	57	16	1.5	0.28	4.16	1.05	0.94	1.36
F1c1	390	0.137	1650	25	3.8	0.12	22.1	2.40	8.85	71.6
F1c2	400	0.032	19	24	2.7	1.30	19.2	1.14	1.82	2.21
F1c3	150	0.030	18	23	2.1	0.83	24.3	0.99	2.11	2.51
F1c4	270	0.063	29	21	2.0	0.87	4.01	0.46	0.74	1.29
F4c5	175	0.060	46	18	2.2	0.54	7.64	0.27	1.33	2.21
F4c7	190	0.024	14	19	1.9	0.59	34.0	0.43	2.39	2.73
H3c3	160	0.042	24	19	2.0	0.64	11.1	0.16	1.35	3.88
H5c3	80	0.042	17	19	1.1	0.41	8.24	0.17	1.00	1.93

[a]From Table 3.

Inspection of Figs 6 and 7 suggests that, overall, there are no strong and clear (anti-)correlations between the $^{14}N/^{15}N$ ratio and the analysed core properties. However, non-parametric statistical tests suggest very tentative positive correlations with the H_2 column density derived from the 3 mm continuum (in Fig. 7). The Pearson's r correlation coefficient is: $r \sim 0.61$ with $N(H_2)^{Her}$ (p-value 0.001); $r \sim 0.58$ with $N(H_2)^{mean}$ (p-value 0.007); $r \sim 0.54$ with $N(H_2)^{peak}$ (p-value 0.01).

We speculate that the positive correlations between the $^{14}N/^{15}N$ ratios and the core column densities could again be the consequence of the selective photodissociation mechanism, already invoked in Section 4.2. In fact, the higher $^{14}N/^{15}N$ average ratio could be due to a larger amount of gas along the line of sight in the core envelope, more exposed to external UV photons responsible for the photodissociation of the $^{14}N^{15}N$ molecule (the parent species of $N^{15}NH^+$) but not of the self-shielded $^{14}N_2$ (parent species of N_2H^+), thus causing an increase in the $^{14}N/^{15}N$ ratio. If we analyse only the star-forming cores, however, we find a tentative positive correlation between $^{14}N/^{15}N$ and the sonic Mach number $\mathcal{M}_S$ ($r \sim 0.76$, p-value 0.004). A tentative difference in $\mathcal{M}_S$, although not statistically significant, was found in paper I between starless and star-forming cores, with the star-forming cores being associated with larger $\mathcal{M}_S$. A very tentative one can be also found between $^{14}N/^{15}N$ and T_{dust} ($r \sim 0.6$, p-value 0.04). Because both parameters are usually associated with gas in a more advanced stage of star formation activity, these tentative correlations could indicate that more evolved cores may be associated with higher $^{14}N/^{15}N$ ratios. However, all trends are strongly influenced by sources F1c1 and F1c2 (Figs 6 and 7). Moreover, most $N^{15}NH^+$ lines are detected with a signal-to-noise ratio in between 3 and 5, and hence any trend that can be found from the plots in Figs 6 and 7 must be taken with caution.

Overall, the fact that we find either no or little correlation between $^{14}N/^{15}N$ and core properties confirm the chemical models of Roueff et al. (2015) and Loison et al. (2019), in which enrichment in ^{15}N is

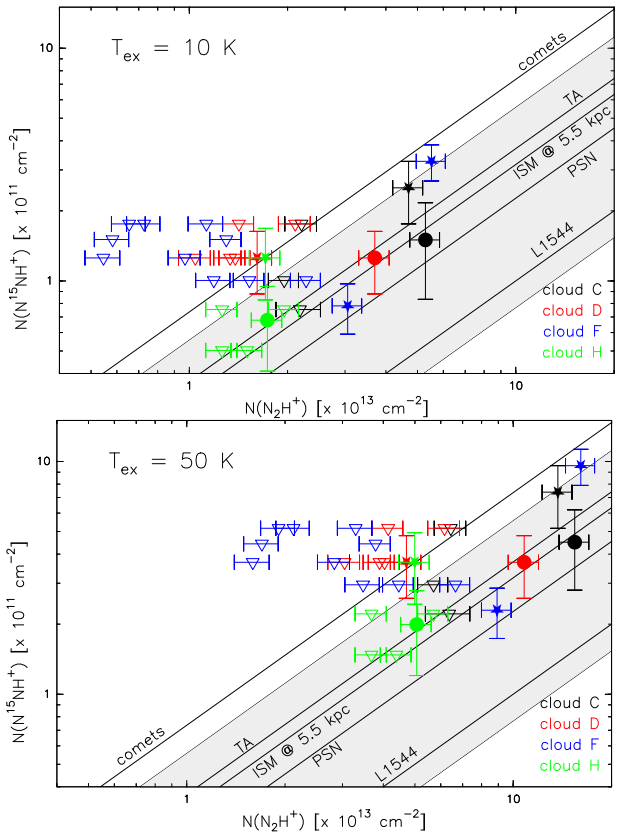

Figure 5. Same as Fig. 4 for the values derived from the spectra extracted from the N_2H^+ cores (see Fig. 1).

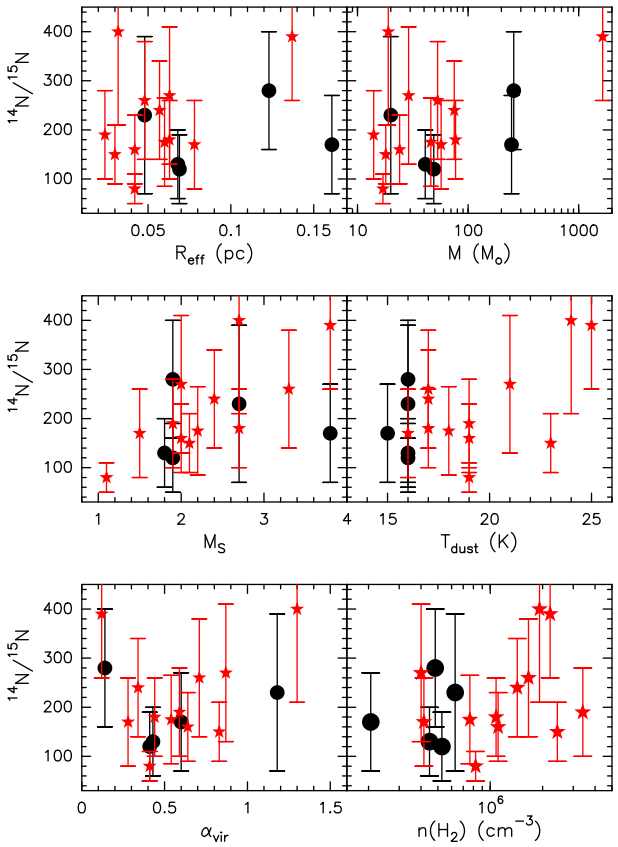

Figure 6. $^{14}N/^{15}N$ ratio of the continuum cores detected in $N^{15}NH^+$ as a function of core physical properties derived in paper I. Specifically, we plot the $^{14}N/^{15}N$ versus: radius (top-left), mass (top-right), Mach number (centre-left), dust temperature (centre-right), virial parameter (bottom-left), and H_2 volume density (bottom-right). In each frame, red stars indicate cores with embedded star-formation activity and black circles indicate the starless cores.

always very low or even negligible for all species formed in the gas phase like N_2H^+. In Loison et al. (2019), a significant ^{15}N enrichment is possible if the gas temperature is below ∼10 K, due to a possibly different exothermicity of the formation reactions of N_2H^+ and $N^{15}NH^+$, not yet experimentally measured (see also Hily-Blant et al. 2020). However, the temperature of our cores at the scales studied by us is always above ∼10 K, in agreement with the lack of ^{15}N enrichment, although the temperature measurement is taken over an angular scale (i.e. the Herschel beam) larger than that of the individual cores. Therefore, in quiescent cores the temperature could be lower on smaller scales, as discussed in paper I.

5 CONCLUSIONS

We have derived the $^{14}N/^{15}N$ ratio from the N_2H^+ and $N^{15}NH^+$ (1–0) lines in a sample of four well-studied IRDCs. The observations, performed with ALMA, represent the first interferometric survey of the $^{14}N/^{15}N$ ratio in cores embedded in IRDCs. The main results are summarized below:

(i) among the 3 mm continuum cores embedded in each IRDC and identified in paper I, we detect 17 out of 62 cores in $N^{15}NH^+$;
(ii) the $^{14}N/^{15}N$ values derived from the column density ratio $N(N_2H^+)/N(N^{15}NH^+)$ in all studied regions are in the range ∼80–400, which roughly goes from the cometary values to the ISM value at the Galactocentric distance of the targets;
(iii) the $^{14}N/^{15}N$ ratios are smaller on average than those found in previous single-dish studies, in which ratios even exceeding ∼1000 are found, suggesting that the $^{14}N/^{15}N$ ratio in the cores is smaller than that in their associated envelope, in agreement with the selective

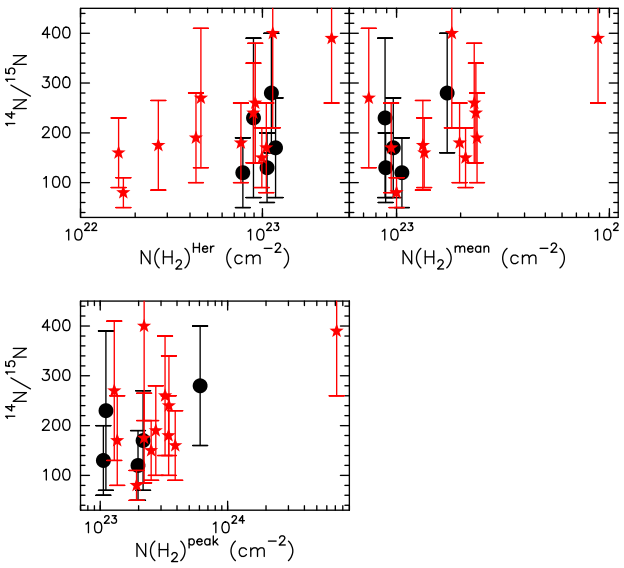

Figure 7. Same as Fig. 6 for the H_2 column densities of the cores calculated from the Herschel continuum (top-left) and from the mean and peak 3 mm continuum emission (top-right and bottom-left, respectively).

photodissociation scenario. The conclusion is strongly supported by the fact that the $^{14}N/^{15}N$ ratios obtained using the total power data only towards the detected cores are on average a factor 1.5–3 higher. This also highlights the need for high-angular resolution measurements to measure accurately the $^{14}N/^{15}N$ ratio in dense cores within IRDCs. However, the sensitivity of our observations likely does not allow us to derive $^{14}N/^{15}N$ ratios higher than ∼400 at small scales. Therefore, higher sensitivity measurements will be absolutely required to confirm, or deny, this finding;

(iv) the average $^{14}N/^{15}N$ ratios in the four clouds (230, 180, 260, 120), are marginally lower (by a factor ∼1.5–2) than the present-day Galactic value at the Galactocentric distance of the clouds (∼300–330);

(v) we find tentative positive trends between $^{14}N/^{15}N$ and H_2 column density of the cores. Among the star-forming clouds only, we also find a tentative positive trend between $^{14}N/^{15}N$ and both the sonic Mach number and the dust temperature. We speculate that this can be due to the selective photodissociation mechanisms, which tends to decrease the $N^{15}NH^+$ abundance, and hence to increase the $^{14}N/^{15}N$ ratio) in cores more exposed to UV photons. The source of these photons is probably external for cores with higher column density, independent on the evolutionary stage of the core. However, due to the fact that the correlations proposed are faint, and that most $N^{15}NH^+$ lines are detected at a significance level of 3–5σ rms in the spectra, any conclusion that can be drawn from these trends must be taken with caution.

ACKNOWLEDGEMENTS

We would like to thank the anonymous referee for their constructive feedback on the manuscript. FF is grateful to Laura Colzi for a very useful discussion. This paper makes use of the following ALMA data: ADS/JAO.ALMA#2017.1.00687.S and ADS/JAO.ALMA#2018.1.00850.S. ALMA is a partnership of ESO (representing its member states), NSF (USA) and NINS (Japan), together with NRC (Canada), MOST and ASIAA (Taiwan), and KASI (Republic of Korea), in cooperation with the Republic of Chile. The Joint ALMA Observatory is operated by ESO, AUI/NRAO and NAOJ. I.J-S has received partial support from the Spanish FEDER (project number ESP2017-86582-C4-1-R) and the Ministry of Science and Innovation through project number PID2019-105552RB-C41. ATB would like to acknowledge funding from the European Research Council (ERC) under the European Union Horizon 2020 research and innovation programme (grant agreement No.726384/Empire).

DATA AVAILABILITY

Data used within this work will be shared on reasonable request to the corresponding author.

REFERENCES

Adams F. C., 2010, ARA&A, 48, 47
Adande G. R., Ziurys L. M., 2012, ApJ, 744, 194
Barnes A. T., Henshaw J. D., Caselli P., Jiménez-Serra I., Tan J. C., Fontani F., Pon A., Ragan S., 2018, MNRAS, 475, 5268
Barnes A. T., Kong S., Tan J. C., Henshaw J. D., Caselli P., Jiménez-Serra I., Fontani F., 2016, MNRAS, 458, 1990
Barnes A. T. et al., 2021, MNRAS, preprint (arXiv:2103.09122)
Bizzocchi L., Caselli P., Leonardo E., Dore L., 2013, A&A, 555, 109
Bockelée-Morvan D. et al., 2008, ApJ, 679, L49
Bonal L., Huss G. R., Krot A. N., Nagashima K., Ishii H., Bradley J. P., Hutcheon I. D., 2010, Geochim. Cosmochim. Acta, 74, 6590
Butler M. J., Tan J. C., 2009, ApJ, 696, 484
Butler M. J., Tan J. C., 2012, ApJ, 754, 5
Caselli P., Myers P. C., Thaddeus P., 1995, ApJ, 455, L77
Caselli P., Walmsley C. M., Zucconi A., Tafalla M., Dore L., Myers P. C., 2002, ApJ, 565, 344
Ceccarelli C., Caselli P., Bockelée-Morvan D., Mousis O., Pizzarello S., Robert F., Semenov D., 2014, in Beuther H., Klessen R. S., Dullemond C. P., Henning Th., eds, Protostars and Planets VI. Univ. Arizona Press, Tucson, p. 859
Colzi L., Fontani F., Caselli P., Ceccarelli C., Hily-Blant P., Bizzocchi L., 2018b, A&A, 609, 129
Colzi L., Fontani F., Caselli P., Leurini S., Bizzocchi L., Quaia G., 2019, MNRAS, 485, 5543
Colzi L., Fontani F., Rivilla V. M., Sánchez-Monge Á., Testi L., Beltrán M. T., Caselli P., 2018a, MNRAS, 478, 3693
Colzi L., Sipilä O., Roueff E., Caselli P., Fontani F., 2020, A&A, 640, 51
Daniel F., Cernicharo J., Dubernet M.-L., 2006, ApJ, 648, 461
Daniel F. et al., 2013, A&A, 560, A3
Daniel F. et al., 2016, A&A, 592, 45
De Simone M. et al., 2018, MNRAS, 476, 1982
Di Francesco J., André Ph., Myers P. C., 2004, ApJ, 617, 425
Dore L., Bizzocchi L., Degli Esposti C., Tinti F., 2009, A&A, 496, 275
Egan M. P., Shipman R. F., Price S. D., Carey S. J., Clark F. O., Cohen M., 1998, ApJ, 494, L199
Endres C. P., Schlemmer S., Schilke P., Stutzki J., Müller H. S. P., 2016, J. Mol. Spec., 327, 95
Fontani F., Busquet G., Palau A., Caselli P., Sánchez-Monge Á., Tan J. C., Audard M., 2015, A&A, 575, 87
Fontani F. et al., 2020, MNRAS, 493, 3412
Fouchet T., Irwin P. G. J., Parrish P., Calcutt S. B., Taylor F. W., Nixon C. A., Owen T., 2004, Icarus, 172, 50
Furuya K., Aikawa Y., 2018, ApJ, 857, 105
Furuya K., Watanabe Y., Sakai T., Aikawa Y., Yamamoto S., 2018, A&A, 615, L16
Füri E., Marty B., 2015, Nat. Geosci., 8, 515
Guzmán V. V., Öberg K. I., Huang J., Loomis R., Qi C., 2017, ApJ, 836, 30
Heays A. N., Visser R., Gredel R., Ubachs W., Lewis B. R., Gibson S. T., van Dishoeck E. F., 2014, A&A, 562, A61
Henshaw J. D., Caselli P., Fontani F., Jiménez-Serra I., Tan J. C., 2014, MNRAS, 440, 2860
Henshaw J. D., Caselli P., Fontani F., Jiménez-Serra I., Tan J. C., Hernandez A. K., 2013, MNRAS, 428, 3425
Hernandez A. K., Tan J. C., Caselli P., Butler M. J., Jiménez-Serra I., Fontani F., Barnes P., 2011, ApJ, 738, 11
Hily-Blant P., Bonal L., Faure A., Quirico E., 2013a, Icarus, 223, 582
Hily-Blant P., Magalhaes V., Kastner J., Faure A., Forveille T., Qi C., 2017, A&A, 603, L6
Hily-Blant P., Pineau des Forêts G., Faure A., Flower D. R., 2020, A&A, 643, 76
Hily-Blant P., Pineau des Forêts G., Faure A., Le Gal R., Padovani M., 2013b, A&A, 557, 65
Jiménez-Serra I., Caselli P., Fontani F., Tan J. C., Henshaw J. D., Kainulainen J., Hernandez A. K., 2014, MNRAS, 439, 1996
Kainulainen J., Tan J. C., 2013, A&A, 549, A53
Kong S., Tan J. C., Caselli P., Fontani F., Liu M., Butler M. J., 2017, ApJ, 834, 193
Lee S., Nomura H., Furuya K., Lee J.-E., 2021, ApJ, 908, 82L
Lichtenberg T., Golabek G. J., Burn R., Meyer M. R., Alibert Y., Gerya T. V., Mordasini C., 2019, Nat. Astraon., 3, 307
Liu M., Tan J. C., Cheng Y., Kong S., 2018, ApJ, 862, 105
Loison J. C., Wakelam V., Gratier P., Hickson K. M., 2019, MNRAS, 484, 2747
Manfroid J. et al., 2009, A&A, 503, 613
Marty B., Zimmermann L., Burnard P. G., 2009, Geochim. Cosmochim. Acta, 73, 842

Marty B., Zimmermann L., Burnard P. G., Wieler R., Heber V. S., Burnett D. L., Wiens R. C., Bochsler P., 2010, Geochim. Coscochim. Acta, 74, 340
McMullin J. P., Waters B., Schiebel D., Young W., Golap K., 2007, ASCP, 376, 127
Perault M. et al., 1996, A&A, 315, L165
Pfalzner S., et al., 2015, Phys. Scr., 90, 068001
Pillai T., Wyrowski F., Menten K. M., Krügel E., 2006, A&A, 447, 929
Portegies Zwart S., Pelupessy I., van Elteren A., Wijnen T. P. G., Lugaro M., 2018, A&A, 616, A85
Redaelli E., Bizzocchi L., Caselli P., Harju J., Chacón-Tanarro A., Leonardo E., Dore L., 2018, A&A, 617, 7
Rodgers S. D., Charnley S. B., 2008, MNRAS, 385, L48
Rosolowsky E. W., Pineda J. E., Kauffmann J., Goodman A. A., 2008, ApJ, 679, 1338
Roueff E., Loison J. C., Hickson K. M., 2015, A&A, 576, 99
Shinnaka Y., Kawakita H., Jehin E., Decock A., Hutsemékers D., Manfroid J., Arai A., 2016, MNRAS, 462, 195
Sokolov V. et al., 2017, A&A, 606, 133
Terzieva R., Herbst E., 2000, MNRAS, 317, 563
Viti S., Fontani F., Jiménez-Serra I., Holdship J., 2019, MNRAS, 486, 4805
Wirström E. S., Charnley S. B., 2018, MNRAS, 474, 3720
Wirström E. S., Charnley S. B., Cordiner M. A., Milam S. N., 2012, ApJ, 757, L11
Zeng S. et al., 2017, A&A, 603, 22

APPENDIX A: SPECTRA

We show in this appendix the spectra extracted from the contours illustrated in Fig. 1.

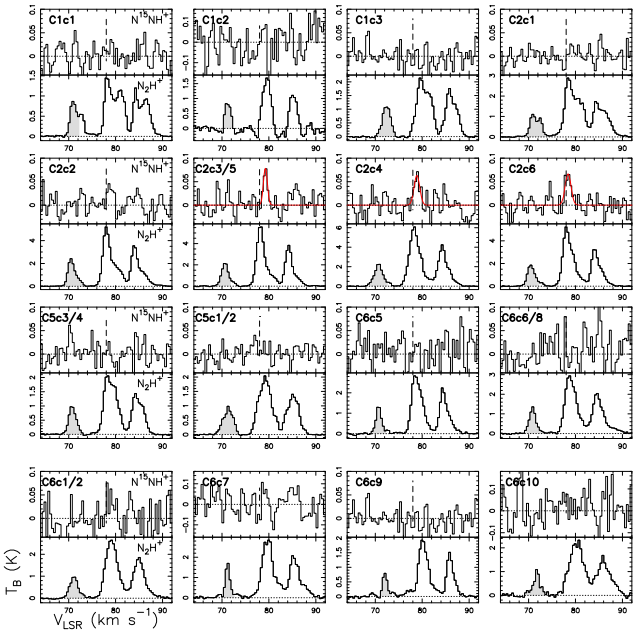

Figure A-1. Spectra of $N^{15}NH^+$ and N_2H^+(1–0) extracted from the 3 mm continuum cores of Cloud C identified in Table 3. In each spectrum, the horizontal dotted line shows the zero-rms level, and the vertical dashed line the systemic cloud velocity (Table 1). The red curves in the $N^{15}NH^+$ spectra are the best fits to the main hyperfine component towards C2c3/5, C2c4, and C2c6 because the hyperfine satellites are not revealed (see Section 3.1.2). The grey region in each N_2H^+ spectrum indicates the integrated intensity used in the calculation of the total column density.

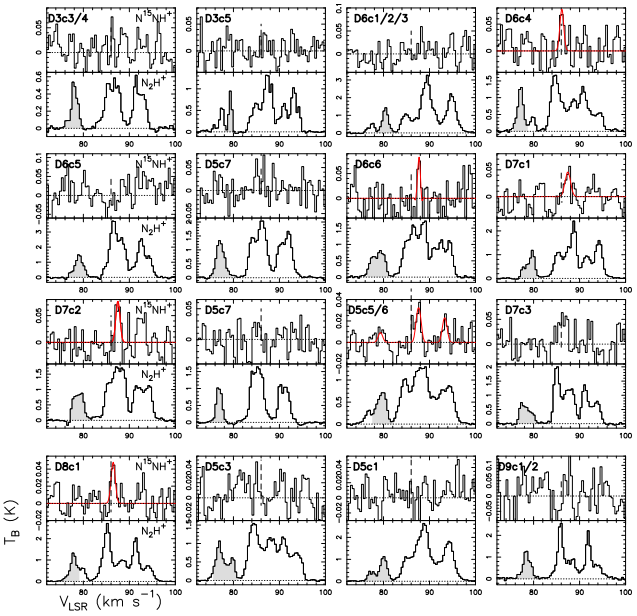

Figure A-2. Same as A-1 for the 3 mm continuum cores in Cloud D in Table 3. Note that for core D5c5/6 we could fit the total hyperfine structure of the $N^{15}NH^+$(1–0) line, and not only the main component.

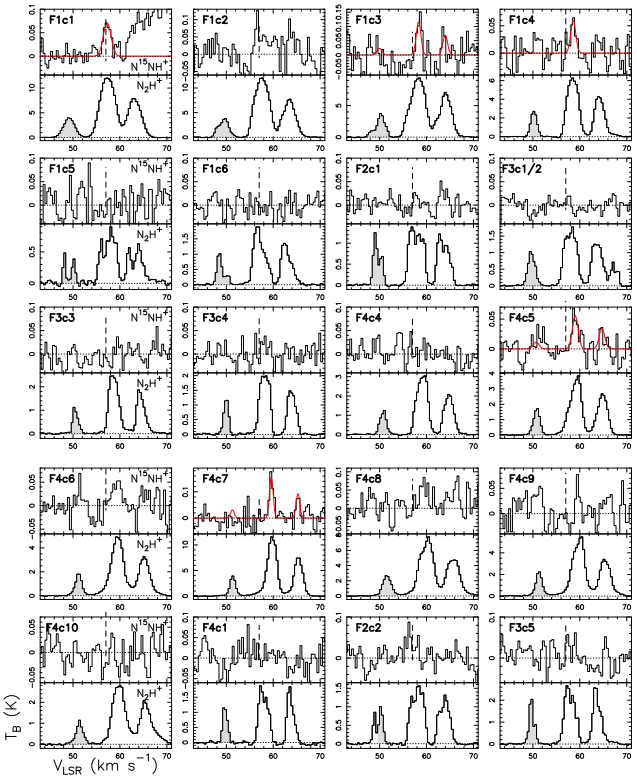

Figure A-3. Same as A-1 for the 3 mm continuum cores in Cloud F in Table 3. Note that we could fit the total hyperfine structure of the $N^{15}NH^+$(1–0) lines of F1c3, F4c5, and F4c7.

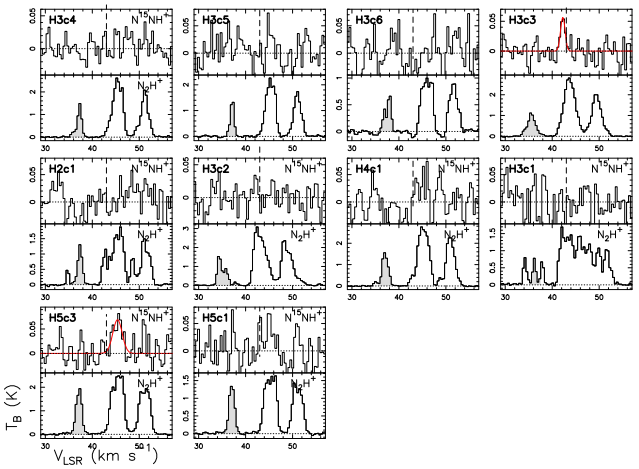

Figure A-4. Same as A-1 for the 3 mm continuum cores of Cloud H.

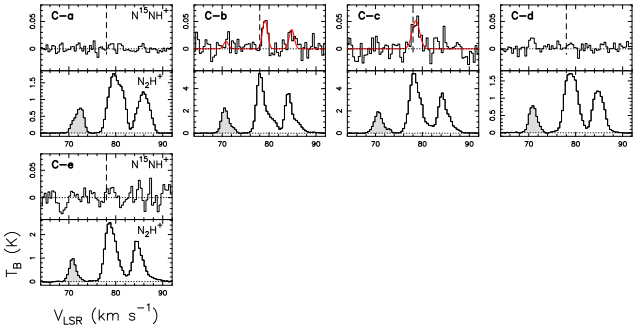

Figure A-5. Spectra of $N^{15}NH^+$ and N_2H^+(1–0) extracted from the N_2H^+ cores of Cloud C (Fig. 1) identified using the dendrogram analysis (paper I). All symbols, lines, and colours have the same meaning as in Fig. A-1.

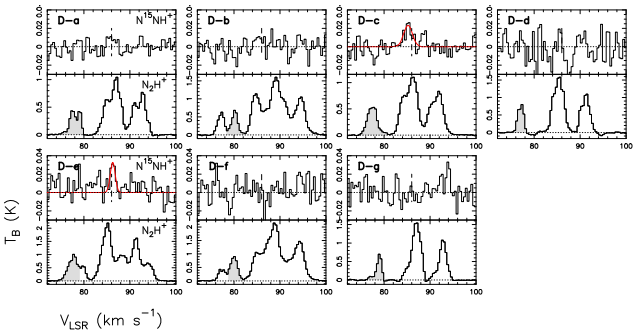

Figure A-6. Same as A-5 for Cloud D.

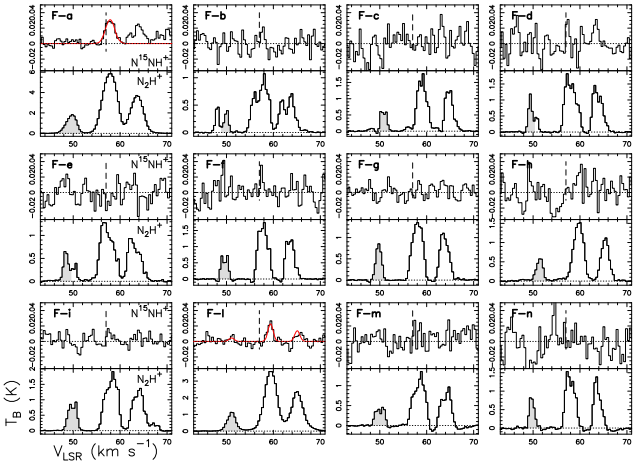

Figure A-7. Same as A-5 for Cloud F.

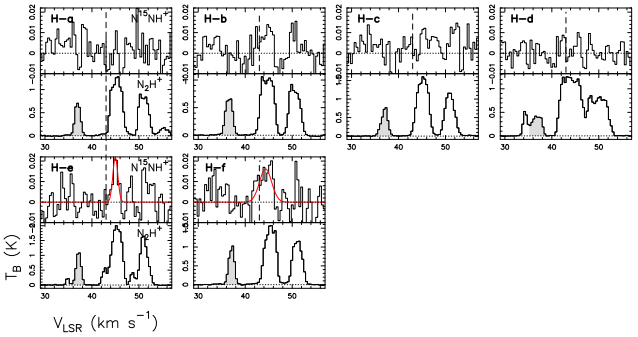

Figure A-8. Same as A-5 for Cloud H.

This paper has been typeset from a TEX/LATEX file prepared by the author.